Chemical Engineering Journal 455 (2023) 140791

Contents lists available at ScienceDirect

Chemical Engineering Journal

journal homepage: www.elsevier.com/locate/cej

A new, efficient and durable MoO_2/Mo_2C-C cocatalyst with the optimized composition and electronic structure via *in-situ* carburization for photocatalytic H_2 evolution

Xiu-Qing Qiao [a,b], Zizhao Wang [a], Chen Li [a], Houfeng Zhang [a], Dongfang Hou [a,b], Ya-Qian Lan [c,*], Dong-Sheng Li [a,b,*]

[a] College of Materials and Chemical Engineering, Key Laboratory of Inorganic Nonmetallic Crystalline and Energy Conversion Materials, China Three Gorges University, Yichang, Hubei 443002, China
[b] Hubei Three Gorges Laboratory, Yichang, Hubei 443007, China
[c] School of Chemistry, South China Normal University, Guangzhou 510006, China

ARTICLE INFO

Keywords:
Photocatalyst
Carbon
Hydrogen
MoO_2/Mo_2C
Cocatalyst

ABSTRACT

Cocatalyst assisted photocatalytic H_2 generation from water under mild conditions can meet the increasing demand for clean and sustainable energy, but efficient and super-stable photocatalyst has rarely been achieved by modulating the composition and structure of cocatalyst. Herein, a fantastic cocatalyst, MoO_2/Mo_2C nanoparticles strongly anchored in conductive carbon matrix (MoO_2/Mo_2C-C), was accurately synthesized by *in-situ* carbonizing strategy and adopted as an efficient and robust cocatalyst for CdS photocatalytic H_2 evolution. To our delight, the obtained MoO_2/Mo_2C-C cocatalyst is extremely stable, retaining the original activity even after two years storage in atmospheric conditions. The optimized MoO_2/Mo_2C-C-CdS-0.3 (MMCC-0.3) photocatalyst, coupling 30 wt% MoO_2/Mo_2C-C with CdS, delivers a substantial H_2 evolution rate of 18.43 mmol h^{-1} g^{-1} and super stability of successive 90 h testing (conducted in 15-day) without a secondary sacrificial agent supplement, as well as a high apparent quantum efficiency of 14.13 %. Both experimental results and DFT calculations reveal that the unique MoO_2/Mo_2C-C cocatalyst not only merited with optimal hydrogen binding energy (ΔG^*) and downshifted d-band center to lower the kinetic barrier of hydrogen evolution reaction, but also promise conductive carbon bridge, high quality interface, and exposed abundant active sites for CdS, which synergistically work with enhanced visible light absorption and promoted charge separation to promise the outstanding activity and stability of MoO_2/Mo_2C-C-CdS photocatalyst. This work not only provides an efficient and low cost cocatalyst for practical application, but also offers valuable insights into the design of robust cocatalyst for photocatalyst and beyond.

1. Introduction

With the acceleration of energy conservation, emission reduction and clean energy, renewable clean energy has gradually become a hot topic in the world energy field as a feasible technical route to promote global energy transformation [1]. Developing sustainable and cleaner energy is a looming challenge [2–4]. Photocatalyst assisted hydrogen evolution reaction (P-HER) was by converting exhaustless solar energy to green hydrogen energy has already been considered to be promising and effective way to solve these problems for its eco-friendly characteristic. Many semiconductors photocatalyst including TiO_2 [5], CdS [6], g-C_3N_4 [7–9], $ZnIn_2S_4$ [10] etc have been explored to effectively decompose water to generate hydrogen. Among them, CdS shows strong competitiveness for the appropriate energy level structure and low cost. However, the efficiency of CdS photocatalyst is restricted by the inherent contradiction between the narrow band gap and fast charge recombination [11]. Cocatalyst decoration could boost the separation of electron-hole and lower the overpotential for P-HER, being turned out to be a pretty up-and-coming strategy for constructing an efficient photocatalytic system [12]. Although Pt-based materials are undisputed state-of-the-art cocatalysts for P-HER, the expensive and scarce characters limit the industrialized application [13]. Substantial efforts have been

* Corresponding authors.
E-mail addresses: yqlan@m.scnu.edu.cn (Y.-Q. Lan), lidongsheng1@126.com (D.-S. Li).

https://doi.org/10.1016/j.cej.2022.140791
Received 27 September 2022; Received in revised form 16 November 2022; Accepted 2 December 2022
Available online 5 December 2022

invested in developing noble metal free cocatalyst, including phosphide, sulfide and carbide [14,15], with some encouraging progress has been achieved. Nevertheless, most of these cocatalyst systems suffer from severe deactivation and instability during the P-HER process due to the strong oxidation of generated holes. To this end, exploiting cost-efficient and stable alternatives for robust noble metals is especially significant and highly imperative.

Molybdenum (Mo)-based materials with special electronic configuration have received ever-increasing attention in photo/electro catalysts and Fenton catalysts [16–22]. Molybdenum oxide (MoO_2) shows incomparable advantages in terms of the chemical stability, high conductivity ($\sim 6 \times 10^3$ S m^{-1}) and metallic properties for the Fermi level (E_F) is localized within the 4d orbital of Mo element. Recently, several works have devoted the exploitation of MoO_2 cocatalyst for photocatalyst [23]. For instance, Yu group recently reported MoO_2 cocatalyst act as holes acceptors to promote the hydrogen production and pyruvic acid synthesis of CdS [24]. Lou group developed ultrasmall MoOx clusters as a novel non-noble cocatalyst to promote the photocatalytic H_2 generation rate of CdS. However, the inferior binding energy with H species, as well as the restricted exposure of active sites for the awkward aggregation at elevated synthesis temperatures is detrimental to the cocatalytic performance. In this perspective, designing and exploring efficient MoO_2 cocatalyst with good dispersity, abundant exposed active sites and optimal electronic structure is of great concern for the construction of competent cocatalyst.

Metal molybdenum carbides (Mo_2C) was also reported to be effective non-Pt cocatalysts for H_2 generation [25,26]. Nevertheless, the lower conductivity of Mo_2C (1.02×10^2 S cm^{-1}) [27] and strong binding energy with H atoms ($\Delta G = -0.8$ eV) [16] hampered the electrons transfer rate and hydrogen-evolution activity. Hence, the optimization of phase and electronic structure to realize the improvement of hydrogen evolution reaction (HER) activity is promising.

Carbon scaffold was generally accepted as support to disperse nanoparticles, boost the conductivity and improve the catalytic performance [28,29]. Nevertheless, most of the carbon matrix was directly introduced, leading to the uneven distribution of nanoparticles and weak interface contact, restricting the improvement of catalytic activity. Aiming at this problem, the *in-situ* formation of carbon support to anchor and disperse cocatalyst nanoparticles is a good way to maximize reaction sites and cocatalytic activity.

From the perspective of cocatalyst functionality, controllably tuning the electronic structure, especially binding energy for adsorbed species and the d-band center of cocatalyst could optimize the cocatalytic activity [30]. However, study on this issue is rare, and the structure–activity relationship of cocatalyst has not yet been sufficiently understood. Hence, artificially tailoring the electronic structure to achieve an efficient cocatalyst is interesting but challenging.

Inspired by the afore-mentioned perspectives, herein, we delicately engineered hybrid MoO_2/Mo_2C NPs highly dispersed on conductive carbon scaffold (MoO_2/Mo_2C-C) by *in-situ* carbonization of MoO_2-C to modulate the electronic structure with facilitated H_2 desorption. Density functional theory (DFT) calculations reveal the carbonization of MoO_2 decreased Gibbs free energy and d-band center of cocatalyst in favor of desorption of hydrogen species. The MoO_2/Mo_2C-C decorated CdS (MMCC) was merited with a highly dispersed cocatalyst, electron transport carbon bridge, high quality interface contact and enhanced visible light absorption, which synergistically promoted the P-HER activity. Benefiting from these virtues, the optimal MMCC-0.3 exhibits a much higher photocatalytic H_2 generation rate (18.43 mmol h^{-1} g^{-1}) than that of MoO_2-C-CdS (10.36 mmol h^{-1} g^{-1}), also exceeding the previously reported other Mo-based cocatalyst decorated photocatalyst. Moreover, stability tests validate both structure and morphology of MoO_2/Mo_2C-C-CdS photocatalyst remains intact after successive 90 h testing. Furthermore, it is surprising to find that the MoO_2/Mo_2C-C cocatalyst retains initial activity even after being stored for 2 years.

2. Experimental section

Cadmium nitrate tetrahydrate ($Cd(NO_3)_2{\cdot}4H_2O$), thiourea (NH_2CSNH_2), ethylenediamine ($C_2H_8N_2$), ammonium molybdate tetrahydrate ($(NH_4)_6Mo_7O_{24}{\cdot}4H_2O$), phenylamine ($C_6H_7N$), methanol ($CH_3OH$), hydrochloric acid (HCl). All used experimental materials were analytical grade and used without further purification.

2.1. Preparation of MoO_2/Mo_2C-C cocatalyst

Typically, 2 mmol $(NH_4)_6Mo_7O_{24}{\cdot}4H_2O$ and 36 mmol phenylamine were dissolved in 40 mL deionized water and then the pH was adjusted to 4.0 by HCl solution. After being stirred at 50 °C for 6 h, white organic–inorganic hybrid precursors $Mo_3O_{10}(C_6H_8N)_2{\cdot}2H_2O$ were collected and served as a self-template to yield cocatalyst. Then, the dried $Mo_3O_{10}(C_6H_8N)_2{\cdot}2H_2O$ precursors were further treated at 775 °C for 2 h with a ramping rate of 5 °C min^{-1} in the flowing N_2 gas atmosphere and the target black MoO_2/Mo_2C-C was obtained. For comparison, MoO_2-C and MoO_2/Mo_2C-Mo were also prepared under 600 °C and 930 °C heat treatment.

2.2. Synthesis of CdS nanorods (NRs)

CdS NRs were synthesized by the solvothermal method. 16.2 mmol $Cd(NO_3)_2{\cdot}4H_2O$ and 48.6 mmol of NH_2CSNH_2 were dissolved in 80 mL of ethylenediamine to get a clear pale green solution. Then the solution was heated in a 50 mL Teflon-lined stainless steel autoclave at 160 °C for 24 h. Finally, bright yellow CdS powder was collected by centrifugation, rinsed and dried.

2.3. Synthesis of the MoO_2/Mo_2C-C-CdS (MMCC) photocatalyst

MoO_2/Mo_2C-C and CdS were mixed by ultrasound method through self-assembly based on the electrostatic interaction between MoO_2/Mo_2C-C and CdS nanorods. The zeta potential of MoO_2/Mo_2C-C at pH 7 was measured to be as −20.8 mV, while the value of CdS nanorod was 8.9 mV and thus the negative charged MoO_2/Mo_2C-C could easily couple with positively charged CdS nanorod to form a heterojunction. The weight percentages of MoO_2/Mo_2C-C were controlled to be 20 wt%, 25 wt%, 30 wt%, 35 wt% and 40 wt%, which are labeled as MMCC-*x* (*x* represents the mass fractions). For comparison, MoO_2-C-CdS, MoO_2/Mo_2C-Mo-CdS, C-CdS and 1 % Pt decorated CdS (Pt-CdS) photocatalysts were also prepared under the same conditions.

2.4. Materials characterization

Thermal analysis of $Mo_3O_{10}(C_6H_8N)_2{\cdot}2H_2O$ was measured on HCT-2 HENVEN microanalyzer in the N_2 atmosphere. The microstructure of the sample was characterized by X-ray diffraction (XRD) on Philips X' Pert Pro diffractometer. X-ray photoelectron spectroscopy (XPS) and ultraviolet photoelectron spectroscopy (UPS) measurements were performed on the ESCALAB 250Xi X-ray photoelectron spectrometer. The X-ray absorption near edge structure (XANES) and extended X-ray absorption fine structure (EXAFS) of the Mo *K-edge* were measured at the 1W1B station in Beijing Synchrotron Radiation Facility operated at 2.5 GeV with a maximum current of 200 mA. Field-emission scanning electron microscopies (FESEM) and energy-dispersive X-ray spectroscopy (EDX) images were realized on JOLJSM-7500F. Transmission electron microscopies (TEM) were performed on JEOL F200 Field emission high resolution transmission electron microscopy. Raman spectra were collected using a Thermo Scientific DXR Micro laser confocal Raman spectrometer with a 532 nm laser diode as the excitation source. BET specific surface areas were analyzed on Microtrac BEL BELSORP-max automatic instrument at 77 K. Fourier transform infrared spectrometer (FTIR) of the samples was recorded with Nexus 670 Thermo Nicolet Fourier transform infrared spectrometer. UV–vis diffuse reflectance

spectroscopy (DRS) was recorded on the Shimazu UV-2550 UV–vis spectrophotometer using $BaSO_4$ as background. Surface photovoltage (SPV) spectroscopy was recorded on a lock-in amplier (SR830) accompanied with a light chopper (SR540). A 500 W Xenon lamp (CHF XQ500W) equipment with a double prism monochromator was used as the light source. The photoluminescence (PL) spectra (F97 Pro) were conducted to analyze the separation of electron-holes of the samples under 320 nm excitation. Fluorescence lifetimes of various photocatalysts were determined by time-resolved fluorescence spectra.

2.5. Photocatalytic H_2 evolution

Photocatalytic H_2 evolution was performed under a 300 W xenon lamp with a 420 nm cut-off filter (Perfect light, China). Typically, 30 mg photocatalyst, 80 mL water and 8 mL lactic acid were poured into a 250 mL Pyrex reaction cell. The system was then pumped to vacuum before the reaction. After the visible light irradiation, the evolved H_2 was detected on a gas chromatograph (GC-9700, China) with a 5 Å molecular sieves column and a thermal conductivity detector (TCD) under N_2 carrier gas. The photocatalyst was continuously used for 90 h except vacuum degassing every 3 h. Once the photocatalytic reaction of a testing cycle was complete, the subsequent cycle was started after degassed to completely remove dissolved gas. The temperature of the mixed liquor was maintained at 25 °C by cyclic water installation during the photocatalytic reaction. The apparent quantum efficiency (AQE) of the sample was determined under the same condition except for the wavelength of incident light. The AQE under monochromatic light was determined according to previous reports [31,32].

2.6. Photo electrochemical tests

Photo-electro-chemical tests were conducted on CHI660E electrochemical workstation with 0.5 M Na_2SO_4 electrolyte solution. Three-electrode system including Ag/AgCl (reference electrode), graphite rod (counter electrode) and sample loaded glassy carbon electrode substrate (working electrode) are equipped. The working electrode was prepared as follows: 4 mg photocatalyst, 7 mL water, 2 mL ethanol and 1 mL Nafion were uniformly mixed together. Then, 5 μL slurry was coated on a pre-cleaned 3 mm glassy carbon electrode and dried in air. Transient photocurrent response (TPR) was obtained under a 300 W Xe lamp light with cut-off filter (λ>420 nm). Mott-Schottky (M−S) plot was conducted at three different frequencies. Electrochemical impedance spectroscopy (EIS) was obtained in 0.1 M KCl solution. The linear sweep voltammetry (LSV) was implemented in 0.5 M H_2SO_4.

2.7. Theoretical calculations

All the density functional theory (DFT) calculations were carried out by using the Vienna ab initio Simulation Package (VASP) [33]. The structures were optimized by considering the model of Mo_2C (1 0 0)/MoO_2 ($\bar{1}$11) according to the HRTEM and XRD results. Perdew-Burke-Ernzerhof (PBE) method based on the generalized gradient approximation (GGA) was adopted to analyze the properties of the material. The cutoff energy for plane wave truncation was selected as 500 eV. The first Brillouin zone uses a 3 × 3 × 1 Monkhorst-Pack (MP) grid for sampling. The interaction between ions and electrons was investigated using the projected augmented wave (PAW) method. The structure optimization process was terminated until the force on each atom was less than 0.02 eV/Å and the energy change was less than 1×10^{-5} eV. The DFT-D3 semi-empirical correction proposed by Grimme was included in the calculation to obtain the correct structure. The Gibbs free energy change (ΔG) for each elemental step is defined as [34]:

$$\Delta G = \Delta E + \Delta ZPE - T\Delta S + \Delta G_U + \Delta G_{pH} \quad (1)$$

where ΔE and ΔZPE represent the calculated adsorption energy and the zero-point energy correction, respectively. T is the temperature. ΔS, U, and ΔG_{pH} are the entropy change, the applied electrode potential, and the free energy correction of the pH, respectively.

The charge density difference was calculated to deeply understand the charge transfer process between MoO_2 and Mo_2C. The difference charge density of the hybrid cocatalyst is defined as follows:

$$\Delta\rho = \rho_{hybrid} - \rho_{MoO_2} - \rho_{Mo_2C} \quad (2)$$

where ρ_{hybrid}, ρ_{MoO2} and ρ_{Mo2C} are the charge densities of the hybrid cocatalyst, MoO_2 and Mo_2C components.

3. Results and discussions

3.1. Synthesis and characterization of photocatalyst

The overall preparation of MMCC photocatalyst was displayed in Fig. 1. Briefly, 1D organic–inorganic hybrid $Mo_3O_{10}(C_6H_8N)_2{\cdot}2H_2O$ precursor, as evidenced by the well matched XRD pattern (Fig. 2a) and SEM image (Fig. S1), was obtained by electrostatic assembly of $C_6H_8N^+$ and $Mo_3O_{10}^{2-}$ under alkaline condition. Here the $Mo_3O_{10}(C_6H_8N)_2{\cdot}2H_2O$ was served as self-sacrificial template for the cocatalyst synthesis. Based on the thermogravimetric curve (Fig. S2) and product analysis (Fig. 2a, Fig. S3–S4), the transformation process of $Mo_3O_{10}(C_6H_8N)_2{\cdot}2H_2O$ precursor can be readily deduced as following Eqs. (3)–(7):

$$C_6H_7N \xrightarrow{N_2} C + H_2\uparrow + N_2\uparrow (220 \sim 480^\circ C) \quad (3)$$

$$[Mo_3O_{10}]\text{clusters} \xrightarrow{N_2} MoO_3 (220 \sim 480^\circ C) \quad (4)$$

$$MoO_3 + C \xrightarrow{N_2} MoO_2 + CO_x\uparrow (\sim 600^\circ C) \quad (5)$$

$$MoO_2 + C \xrightarrow{N_2} Mo_2C + CO_x\uparrow (\sim 775^\circ C) \quad (6)$$

$$MoO_2 + Mo_2C + C \xrightarrow{N_2} Mo + CO_x\uparrow (\sim 930^\circ C) \quad (7)$$

Obviously, hybrid MoO_2/Mo_2C anchored on carbon matrix (MoO_2/Mo_2C-C) can be obtained by partially *in-situ* carbonization of MoO_2, which promises the formation of high quality interface between compositions. After that, MoO_2/Mo_2C-C-CdS (MMCC) photocatalyst was obtained by ultrasonic mix MoO_2/Mo_2C-C cocatalyst and the as-prepared CdS NRs.

XRD patterns and Raman spectra were applied to identifying the composition and phase of cocatalyst. The XRD pattern in Fig. 2a indicates the products obtained at 600 °C, 775 °C and 930 °C are MoO_2-C, MoO_2/Mo_2C-C and MoO_2/Mo_2C-Mo, respectively. As for MoO_2/Mo_2C-C, the XRD diffraction peaks can be well indexed to the monoclinic MoO_2 (JCPDS No. 32–0671) and cubic Mo_2C (JCPDS No. 15–0457), respectively. The carbon species was evidenced by the Raman spectrum in Fig. 2b. Two characteristic Raman peaks at 1360.4 and 1592.2 cm^{-1} can be attributed to the D-band of disordered carbon (A_{1g} vibration mode) and G-band of graphite carbon (E_{2g} vibration mode), confirming the existence of amorphous and graphite carbon [35,36]. In addition, Mo-O-Mo stretching vibration (816.3 cm^{-1}), Mo = C bond in Mo_2C (663.7 and 995.3 cm^{-1}), vibration modes of Mo-O in MoO_2 (566.5 and 729.4 cm^{-1}), and phonon vibration in MoO_2 (199.1, 226.1, 280.8, 337.9, 354.3, 376.5 and 489.3 cm^{-1}) indicate the presence of MoO_2 and Mo_2C in the cocatalyst [37–39].

SEM image of MoO_2/Mo_2C-C cocatalyst in Fig. 2c displays well scattered MoO_2/Mo_2C NPs are anchored on carbon scaffold. TEM image in Fig. 2d further confirms the well inherited one-dimensional precursor morphology with dispersed nanoparticles. These bright spots in selected area electron diffraction (SAED) pattern (Fig. 2e) are indexed to highly crystallized MoO_2 and Mo_2C NPs. No obvious lattice fringes of carbon matrix were observed in HRTEM images (Fig. 2f) for the amorphous structure, agreeing well with the XRD and Raman analysis. HRTEM

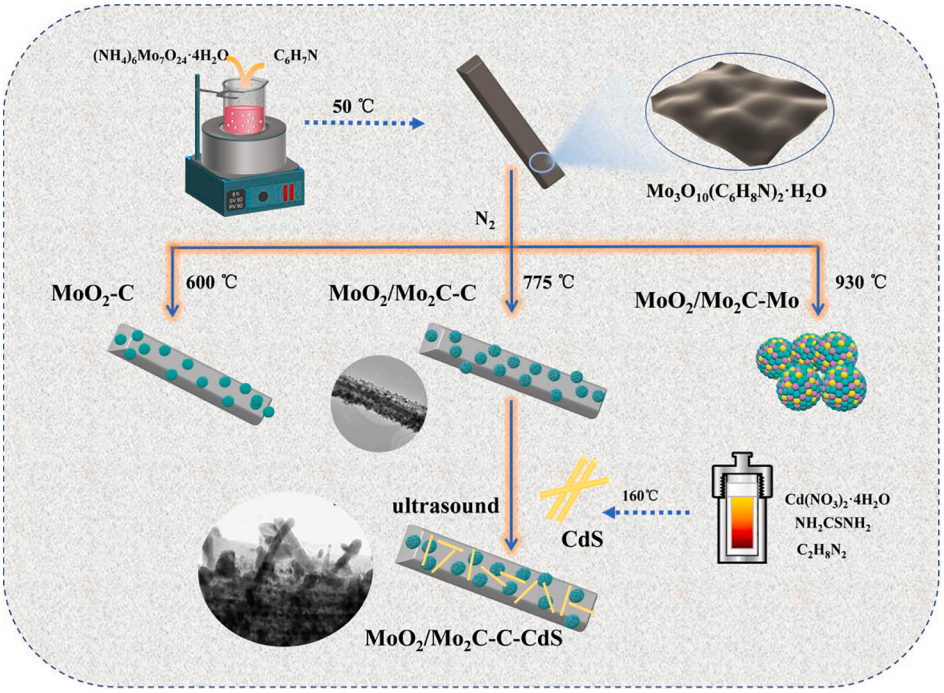

Fig. 1. Schematic illustration of the synthesis of MoO_2/Mo_2C-C-CdS (MMCC) photocatalyst.

image in Fig. 2g displays partial MoO_2/Mo_2C NPs are encapsulated in carbon matrix. The clear lattice fringes with spacing of 0.342 nm and 0.207 nm in Fig. 2g are ascribed to the$(11\bar{1})$ plane of MoO_2 and (200) plane of Mo_2C, respectively. The observed high-quality contact guarantees the fast charge carriers transfer between the different components. The high-angle annular dark-field scanning TEM (HAADF-STEM) image (Fig. 2i) and energy-dispersive X-ray spectroscopy (EDX) elemental mappings (Fig. 2j-m) evidence the MoO_2/Mo_2C NPs are highly and uniformly dispersed on the carbon matrix. The conductive carbon not only prevents the aggregation of cocatalyst but also provides "highways" for charge carriers' transportation, which will benefit the separation of charge carriers.

X-ray absorption structure (XAS) of Mo *K-edge* was applied to reveal the chemical state and local coordination environment of Mo species in MoO_2-C and MoO_2/Mo_2C-C. The X-ray absorption near edge structure (XANES) in Fig. 3a indicates that MoO_2-C has the highest energy absorption edge (E_0) due to a higher oxidation state [40,41]. The E_0 of Mo species in the MoO_2/Mo_2C-C sample is located between that of Mo foil and MoO_2-C, indicating Mo is positively charged and the average chemical valence is between Mo^0 and Mo^{4+} [42]. The overall features of the Mo *K-edge* in MoO_2/Mo_2C-C strongly resemble that of MoO_2-C, revealing a similar coordination structure. The corresponding Fourier transformed (FT) k^3-weighted $\chi(k)$ function of extended XAFS (FT-EXAFS) curves are plotted in Fig. 3b. The peak at 2.36 Å (without phase corrected) for Mo-foil originates from the Mo-Mo backscattering coordination. In light of the MoO_2-C sample, two main peaks at 1.56 and 3.34 Å can be ascribed to Mo-O and Mo–Mo in the first and second coordination shells [43,44], respectively. The weak peak at 2.17 Å originates from Mo-Mo backscattering. As for MoO_2/Mo_2C-C, the peak at 1.56 Å can be fitted to Mo-C/O contributions [45], which is difficult to distinguish because of the similar bond lengths of Mo–O and Mo–C. However, the shorter Mo–Mo bond in MoO_2/Mo_2C-C is caused by the C atoms doped into the MoO_2. Moreover, the amplitude of this peak is greatly increased compared to that of MoO_2-C for the scattering contributions of Mo-C coordination. The well-resolved peaks at 2.14 Å (Mo–Mo) and 3.19 Å (Mo–Mo) reveal similar scattering paths to the MoO_2-C. The determined coordination number of C/O atoms surrounding the Mo scatting center is 2.00 ± 0.34 by the quantitative fitting of the FT-EXAFS spectrum in R space (Fig. 3c and d, Table S1). The average distance of Mo-C/O shell is 2.00 ± 0.03 Å. The first derivatives of XANES at Mo *K-edge* of the samples were analyzed to reveal the electron density of Mo species and the plots are depicted in Fig. 3e. The observed maximum value of MoO_2/Mo_2C-C (20003.1 eV) is located between Mo foil (20000.0 eV) and MoO_2-C (20008.8 eV), further indicating the oxidization state of Mo species [46,47]. Fig. 3f exhibits the relationship between half-energy and valence state of Mo *K-edge* [48]. The average oxidation state of Mo in MoO_2/Mo_2C-C is estimated to be + 1.75 by liner-fitting, indicating Mo is in electron deficient state [48]. Wavelet transforms EXAFS (WT-EXAFS) of Mo *K-edge* EXAFS oscillations based on Morlet wavelets was performed to reveal the radial distance resolution in the *R* and *k* space [49,50]. As shown in Fig. 3g, the intensity maximum at ~8.2 $Å^{-1}$ for Mo foil could be assigned to the Mo-Mo contribution. The intensity maximum at ~4.4 and ~12.3 $Å^{-1}$ for MoO_2-C are assigned to Mo-O and Mo-Mo contributions. For MoO_2/Mo_2C-C, the WT maximum center at ~6.5 $Å^{-1}$ corresponds to Mo-C/O while another at ~11 $Å^{-1}$ associates with Mo-Mo contribution, evidencing the formation of MoO_2 and Mo_2C in the sample.

The obtained MoO_2/Mo_2C-C cocatalyst was then coupled with CdS NRs to evaluate the cocatalytic activity. XRD (Fig. 4a), SEM (Fig. S5a) and TEM images (Fig. 4b and c) of CdS photocatalyst indicate the successful preparation of well crystallized CdS NRs. XRD diffraction patterns of all MMCC samples in Fig. 4a illustrate the MoO_2/Mo_2C-C cocatalyst decoration not change the crystal structure of CdS NRs. In the XRD patterns of MMCC photocatalysts, a small peak at 26.03° corresponding to the $(\bar{1}11)$ plane of MoO_2 can be identified. Moreover, the diffraction peak of MoO_2 slightly shifted to a lower value while the peak of CdS shifted to a higher value, which indicates a strong interface couple exists between MoO_2 and CdS. SEM (Fig. 4d, Fig. S5b) and TEM (Fig. 4e) images of MMCC-0.3 sample indicate both MoO_2/Mo_2C NPs and CdS NRs are well-dispersed on the carbon matrix while some CdS NRs exist alone. HRTEM images in Fig. 4f and g forcefully testify the close interface contact between MoO_2/Mo_2C NPs, carbon matrix and CdS NRs. The STEM image (Fig. 4h) and corresponding elemental mappings (Fig. 4i–n) of MMCC-0.3 reveal the homogeneous distribution of CdS NRs and MoO_2/Mo_2C NPs over the entire carbon matrix. These results indicate MMCC photocatalyst with high quality interface contact

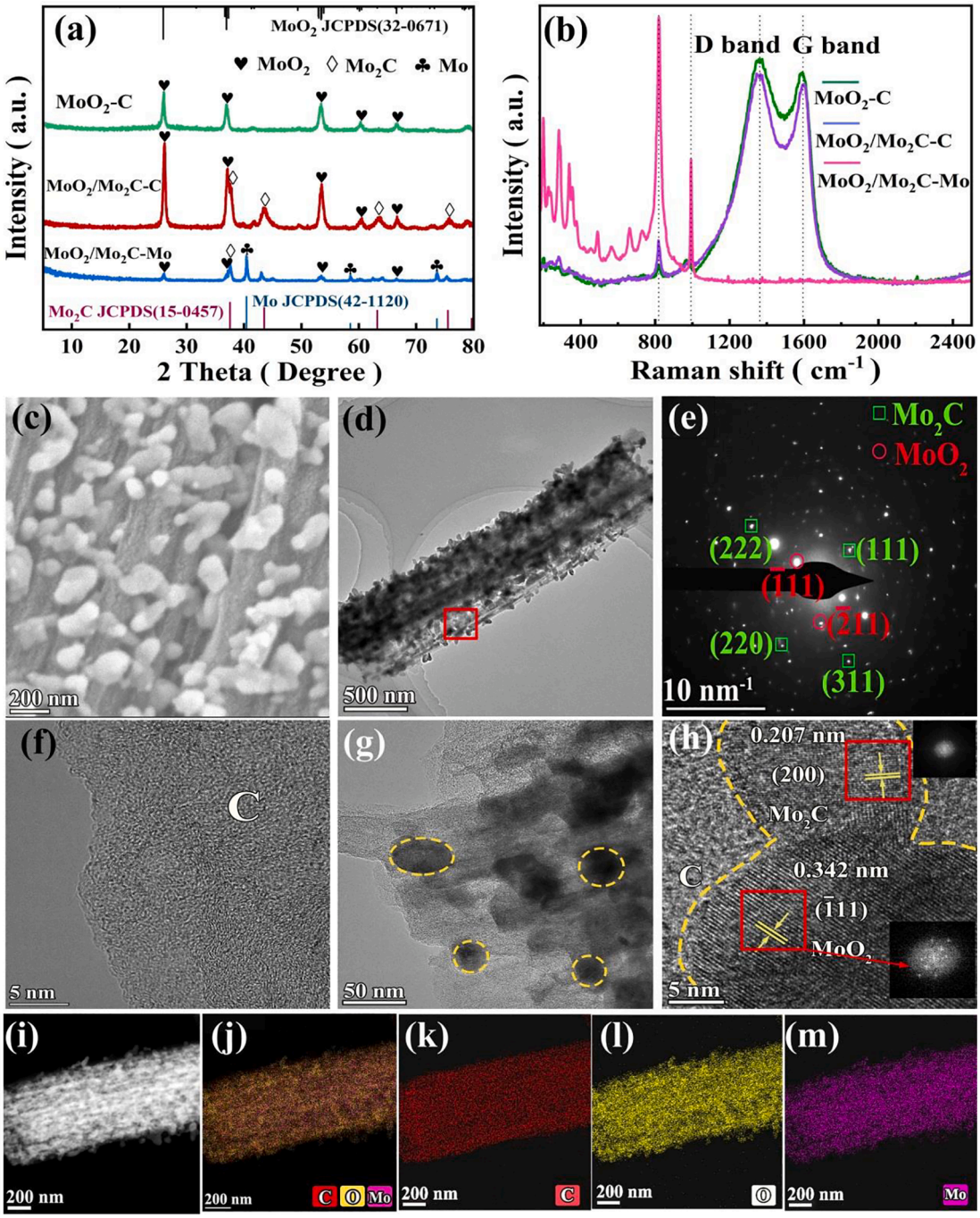

Fig. 2. a) XRD patterns and (b) Raman spectra of different cocatalysts. c) SEM, d) TEM, (e) SAED pattern of the region labled by red line, (f-h) HRTEM, (i) HAADF-STEM image and corresponding EDS elemental mappings (j-m) of MoO_2/Mo_2C-C cocatalyst.

is successfully constructed.

XPS survey spectrum was further analyzed to testify the composition and chemical valence states of the MMCC-0.3 photocatalyst. As plotted in the XPS survey spectrum (Fig. 5a), the MMCC sample is composed of C, Mo, O, S and Cd elements. The C 1 s signal of MoO_2/Mo_2C-C cocatalyst in Fig. 5b can be deconvoluted into three peaks: 284.8, 286.1 and 288.4 eV, corresponding to C—C, C—O single and C═O double bond, respectively [38,51]. The existence of C—O bond proves the strong interface interaction between MoO_2 and carbon matrix [52]. For MMCC-0.3 photocatalyst, the corresponding binding energies are centered at 284.8, 286.4 and 288.5 eV, respectively. Obviously, compared with MoO_2/Mo_2C-C cocatalyst (286.1 eV and 288.4 eV), the C 1 s binding energy of the MMCC-0.3 sample (286.4 eV and 288.5 eV) shifted positively, indicating interfacial interaction between CdS and MoO_2/Mo_2C-C cocatalyst. Fig. 5c reveals the Mo 3d orbitals with four typictal peaks. As for MoO_2/Mo_2C-C, the peaks at 236.2 eV and 233.1 eV can be assigned to Mo $3d_{3/2}$ and Mo $3d_{5/2}$ of Mo^{4+} in MoO_2, whereas the binding energies centered at 231.7 eV and 228.7 eV suggest the existence of Mo^{2+} (Mo-Mo bond) [38,53,54] in Mo_2C, respectivly. As for MMCC-0.3 sample, due to the strong interaction between cocatalyst and CdS, the peaks for Mo^{4+} (235.6 eV and 232.5 eV) and Mo^{2+} (231.1 eV and 228.1 eV) are slightly shifted negativly. The new peak at 226.1 eV is from the S 2 s in CdS [32]. Regarding the O1s in Fig. 5d, there are three peaks at 531.0 eV, 532.2 and 533.4 eV in MoO_2/Mo_2C-C. The peak at 531.0 eV corresponds to the lattice oxygen O^{2-} in the MoO_2 [55], while the bind energy at 532.2 eV may be associated with the oxygen ions in

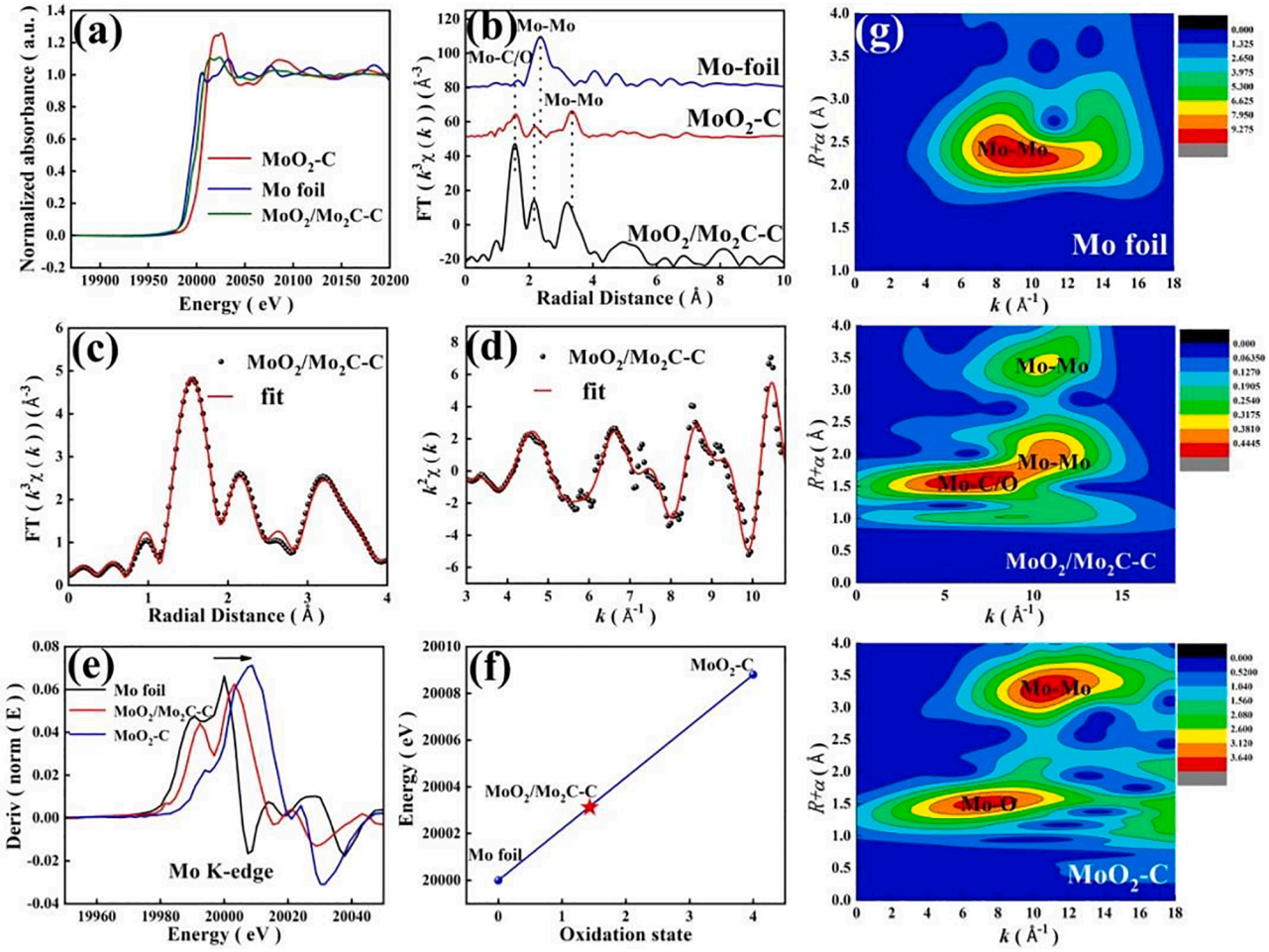

Fig. 3. a) XANES and b) Mo *K-edge* FT-EXAFS for MoO_2/Mo_2C-C, MoO_2-C along with Mo foil reference sample. EXAFS fitting curve of MoO_2/Mo_2C-C at (c) R space and (d) k^3 weighted k-space. e) The first derivatives of XANES at Mo *K*-edge. f) Relationship between half step energy and oxidation state of the Mo species. g) WT-EXAFS of Mo *K-edge* EXAFS oscillations.

the low coordination or defective vacancy sites of the materials [56]. The peak at 533.4 eV comes from absorbed oxygen species. The relatively lower O1s spectrum in MMCC-0.3 photocatalyst is caused by the relatively low content of MoO_2/Mo_2C-C in MMCC photocatalyst, corresponding with the XRD results. It is noteworthy that the relative intensity of lattice oxygen O^{2-} in MMCC photocatalyst significantly decreased while the vacancies O^{2-} increased, which may be caused by the oxygen loss from the lattice under ultrasound effect [57]. In comparison, the O1s binding energy of the MMCC-0.3 photocatalyst present different degrees of negative-shift, verifying the increased electron density of cocatalyst. As observed in Fig. 5e, the Cd $3d_{3/2}$ and Cd $3d_{5/2}$ in the CdS are located at 411.6 and 404.9 eV [58], while the values for MMCC-0.3 are 412.1 and 405.4 eV respectively. In Fig. 5f, the two peaks at 162.3 and 161.1 eV corespond to the S $2p_{1/2}$ and S $2p_{3/2}$ of CdS, respectivly [59]. As for MMCC-0.3 photocatalyst, both the Cd 3d and S 2p orbitals are shifted postively for the decreased electron density. The opposite electron transfer direction convincingly demonstrates strong interface interaction exist between MoO_2/Mo_2C-C cocatalyst and CdS, which effectivly benefit the charge transfer and hence acclearate the photocatalytic H_2 evolution activity. Moreover, FT-IR (Fig. S6) and Raman spectra (Fig. S7) indicate the similar features of CdS before and after cocatalyst introduction. The slightly increased specific surface areas and pore structure (Fig. S8, Table S2) indicate the introduction of MoO_2/Mo_2C-C cocatalyst exerts only negligible effect on the CdS.

3.2. Photocatalytic H_2 evolution activity

To evaluate the activity of MoO_2/Mo_2C-C cocatalyst, photocatalytic H_2 evolution activity of MMCC sample was estimated, along with MoO_2-C, MoO_2/Mo_2C-Mo, C and commercial platinum carbon modified CdS studied for comparison. As shown in Fig. 6a, CdS alone exhibits low H_2 evolution rate of 3.78 mmol h^{-1} g^{-1}, while no H_2 evolution was detected for MoO_2/Mo_2C-C cocatalyst. When combine MoO_2/Mo_2C-C with CdS, a remarkably improved H_2 evolution rate was achieved, indicating MoO_2/Mo_2C-C merely act as co-catalyst for photocatalytic H_2 evolution. Among the MMCC photocatalyst, MMCC-0.3 sample offers the highest H_2 production rate of 18.43 mmol h^{-1} g^{-1}, which is 4.87-fold enhancement with respect to bare CdS. The H_2 generation rate decreased for higher cocatalyst content due to the "shielding effect" of photocatalyst [60]. Fig. 6b compares the photocatalytic H_2 evolution rate of various cocatalyst modified CdS. Significantly, the MMCC-0.3 exhibits much higher photocatalytic activity than other cocatalyst modified CdS, including MoO_2-C-CdS (10.36 mmol h^{-1} g^{-1}), MoO_2/Mo_2C-Mo-CdS (15.52 mmol h^{-1} g^{-1}) and C-CdS (5.15 mmol h^{-1} g^{-1}), even close to the state-of-the-art 1 wt% platinum carbon modified CdS (Pt-CdS, 19.58 mmol h^{-1} g^{-1}), indicating the absolutely essential function of MoO_2/Mo_2C NPs and carbon matrix for the superior photocatalytic activity of MMCC photocatalyst.

Apart from the H_2 evolution rate, the long-term stability is equally important for a practical photocatalyst [61]. Fig. 6c presents the durability test of MMCC-0.3 photocatalyst. Obviously, the MMCC-0.3 shows

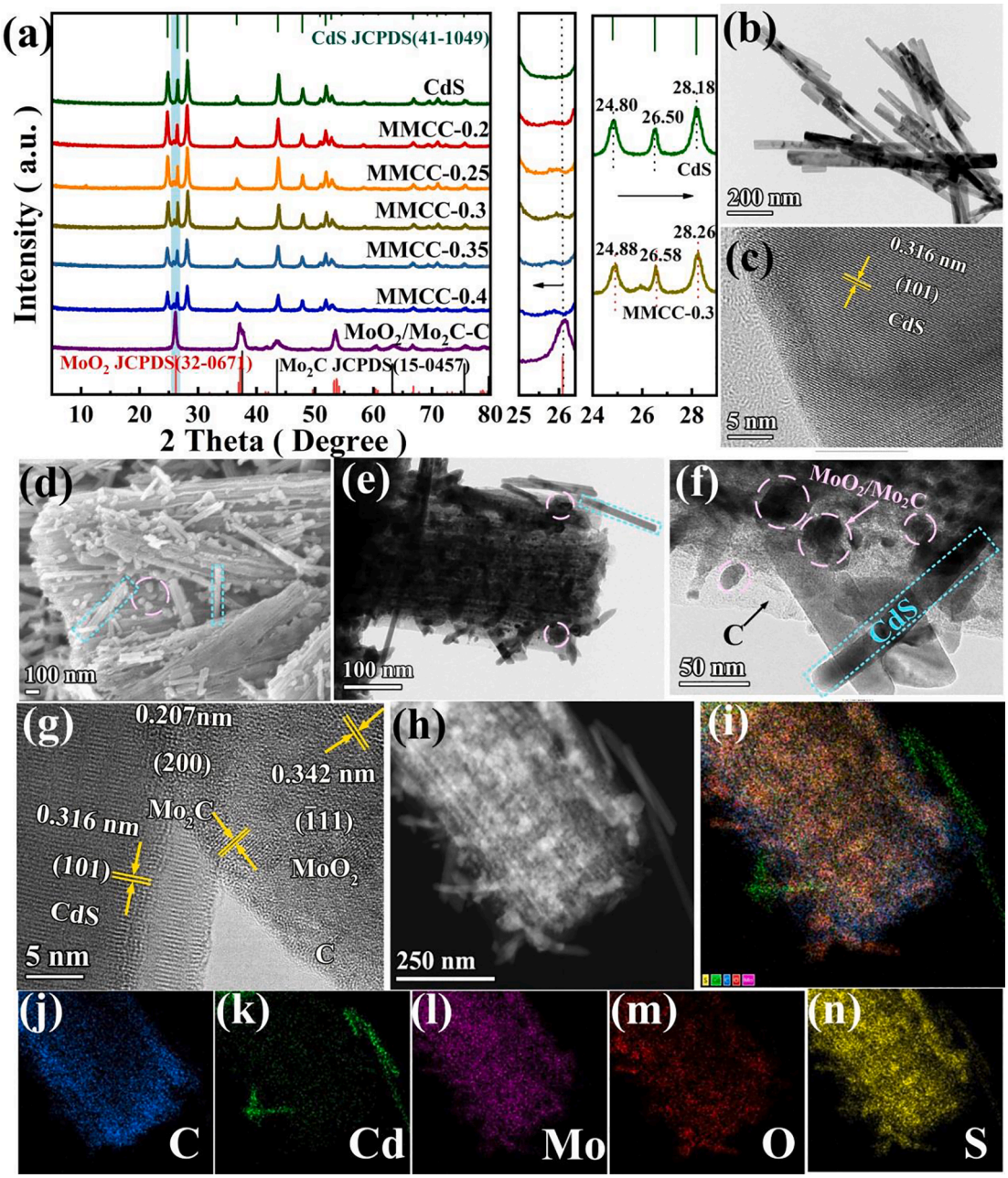

Fig. 4. (a) XRD patterns of CdS, MoO_2/Mo_2C-C cocatalyst, and MMCC composites. (b) TEM and (c) HRTEM images of CdS NRs. (d) SEM, (e) TEM, (f-g) HRTEM images, (h) STEM image and the corresponding elemental mapping images of C, Cd, Mo, O and S elements of MMCC-0.3 photocatalyst (i-n).

identical H_2 evolution activity during continuous 90 h long-term durability measurement (conducted in 15-day) without a secondary sacrificial agent supplement, indicating the excellent stability. Excitingly, the activity of MoO_2/Mo_2C-C cocatalyst can be well retained even after 2 years of storage under atmospheric conditions. Moreover, the XRD pattern (Fig. 6d), SEM image (Fig. S9), XPS spectra (Fig. 6e and f, Fig. S10) and TEM images (Fig. 6g, Fig.S11) of used MMCC-0.3 photocatalyst with negligible change, further reveals the structure stability nature of MMCC-0.3 photocatalyst. In contrast, the H_2 evolution rate of control samples deteriorated seriously during 18 h (Fig. 6h). The photocatalytic H_2 evolution rate of MoO_2/C-CdS decreases by 64.6 %, while MoO_2/Mo_2C-Mo-CdS decreases by 55.0 % in successive 6 runs, respectively. This result indicates the absolutely essential functions of MoO_2/Mo_2C NPs and carbon matrix for the superior stability of MMCC-0.3 photocatalyst. In this case, carbon matrix may not only serve as fast electron delivery channel but also protect the cocatalyst from photo erosion by embedding partial MoO_2/Mo_2C. Moreover, the wavelength-dependent apparent quantum efficiency (AQY) value in Fig. 6i indicates the enhanced electron utilization efficiency for MMCC-0.3 photocatalyst, with the value reaching 14.13 % under 440 nm. To our delight, the P-HER activity and AQY value rank the reported state-of-the-art Mo-based co-catalyst (Table S3) and non-noble metal co-catalyst modified CdS photocatalysts (Table S4). Consequently, Mo_2C not only could enhance the cocatalytic activity of MoO_2 but also promise super long-term stability, which is crucially important for practical application.

3.3. Photocatalytic mechanism discussion

To explore the essential reasons of remarkable activity for MoO_2/Mo_2C-C cocatalyst, First-principle DFT calculation was performed to uncover the intrinsic influence of Mo_2C on MoO_2 cocatalytic activity. The optimized geometric structure of MoO_2 ($\bar{1}11$)/Mo_2C (100) was

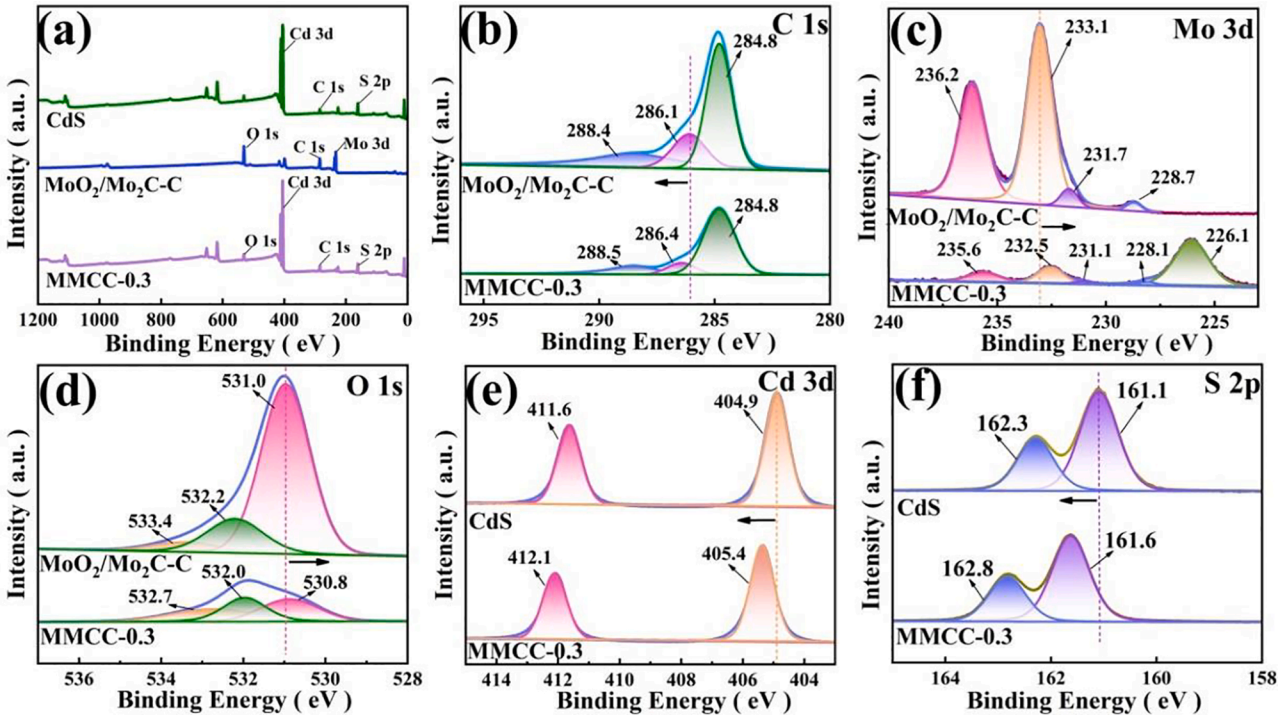

Fig. 5. (a) XPS survey spectra of CdS NRs, MoO_2/Mo_2C-C cocatalyst and MMCC-0.3 photocatalyst. High resolution XPS spectra of (b) C 1 s, (c) Mo 3d, (d) O 1 s, (e) Cd 3d and (f) S 2p of CdS NRs, MoO_2/Mo_2C-C cocatalyst and MMCC-0.3 photocatalyst.

shown in Fig. 7a–c. The hydrogen adsorption Gibbs free energy (ΔG_{H^*}) of catalyst is generally accepted to determine the P-HER activity. Since $|\Delta G_{H^*}|$ reflects the reversible desorption of H* from the active sites, an ideal cocatalyst should have the value of $\Delta G_{H^*} \approx 0$ [62–64].As shown in Fig. 7d, the MoO_2/Mo_2C hybrid cocatalyst exhibits a much lower $|\Delta G_{H^*}|$ value (0.15 eV) than MoO_2 (0.59 eV) and Mo_2C (0.85 eV), very close to ideal Pt (0.10 eV), indicating the positive role of Mo_2C to promote the cocatalytic performance. The zero-approaching $|\Delta G_{H^*}|$ facilitates the H adsorption/desorption process and promises it great superiority for excellent photocatalytic H_2 evolution performance.

In order to deeply understand the electronic coupling interaction in the Mo_2C/MoO_2 heterojunction, the differential charge density at the interface was analyzed. As shown in Fig. 7e, the distinct charge distribution at the interface indicates a strong electronic interaction between MoO_2 and Mo_2C. The yellow and cyan regions represent the charge accumulation and deletion, respectively. Careful analysis reveal that electrons are transferred from MoO_2 to Mo_2C, thus optimizing the electronic structure and $|\Delta G_{H^*}|$, leading to the promoted separation of photo-generated charges. Moreover, the density of states (DOS) was further investigated to uncover the electronic interaction between cocatalyst and adsorbate [65]. As shown in Fig. 7f, the Fermi level of MoO_2 passed through the conduction band, verifying the metallic characteristic [66]. Moreover, the enhanced localized states density near the Fermi level of MoO_2/Mo_2C (Fig. 7g) indicates the improved intrinsic electrical conductivity and thus guarantees the fast electron transfer [67], contributing to the enhanced P-HER activity. The d-band center model has been used to explain the catalytic activity of transition metal [68,69]. Generally, the orbit of adsorbates will couple with d state of transition-metal and result the splitting of energy level, giving rise to the formation of bonding state and antibonding states. Bonding state is always occupied, while antibonding is partially occupied. The probability of electron filling in the antibonding states depends on the relative position of the orbitals to the Fermi level. The higher the d-band of the transition metal and the antibonding state energy, the lower the occupied degree, hence the stronger the chemical binding between the transition metal and adsorbates. Therefore, the P-HER activity of the catalyst could be tuned by tailoring the position of the d-band center. As shown in Fig. 7h and i, the d-band centers of MoO_2/Mo_2C heterojunction and MoO_2 are located at −1.27 eV and −1.15 eV, respectively, indicating the d-band center is downshifted and far away from the Fermi level after the formation of Mo_2C. Hence, the antibonding state is reduced and more electrons will be filled in [68]. As a result, the interaction between cocatalyst and adsorbate is weakened and the desorption of H* from the surface of cocatalyst is facilitated to promote the H_2 evolution.

Apart from the optimized $|\Delta G_{H^*}|$ value and d-band center of MoO_2/Mo_2C, the optical and electrochemical properties of MMCC-0.3 photocatalyst was further explored to gain insight into the accurate mechanism of fantastic cocatalytic activity. UV–vis DRS spectrum of all the samples in Fig. 8a with absorption band edges at 520 nm was caused by the intrinsic absorption of pure CdS. Strong continuous light absorption of MoO_2/Mo_2C-C cocatalyst between 400 ~ 800 nm suggests the metallic nature of MoO_2/Mo_2C-C cocatalyst [70], consists with DFT results. The visible light absorption abilities of MMCC samples enhanced significantly due to the decoration of MoO_2/Mo_2C-C cocatalyst, corresponding well with the color change (inset in Fig. 8a). The determined band gaps (*Eg*) by the expression : $[(\alpha h\nu)^2 = A(h\nu - E_g)$ for CdS is 2.30 eV [71].

Mott-Schottky plots are conducted to ascertain the band structure of the sample based on the Mott–Schottky function in Eq.(8):

$$\frac{1}{c^2} = \frac{2}{A^2 \varepsilon \varepsilon_0 q N_D}\left(E - E_{FB} - \frac{k_B T}{q}\right) \quad (8)$$

Here, C is the space charge layer capacitance; k_B is the Boltzmann constant; A is the interfacial area b; ε and ε_0 are dielectric constant of CdS and vacuum permittivity (8.85×10^{-14}F m^{-1}); N_D is the carrier density; q is the elementary charge (1.6×10^{-19}C); E is the implemented potential; E_{FB} is the flat-band potential and T is the absolute temperature.

M−S plots in are plotted in Fig. 8b, the positive slope in the plots of C_s^{-2} versus external voltage indicates the n type characteristic of CdS photocatalyst. The flat potential (E_{fb}) can be determined from the

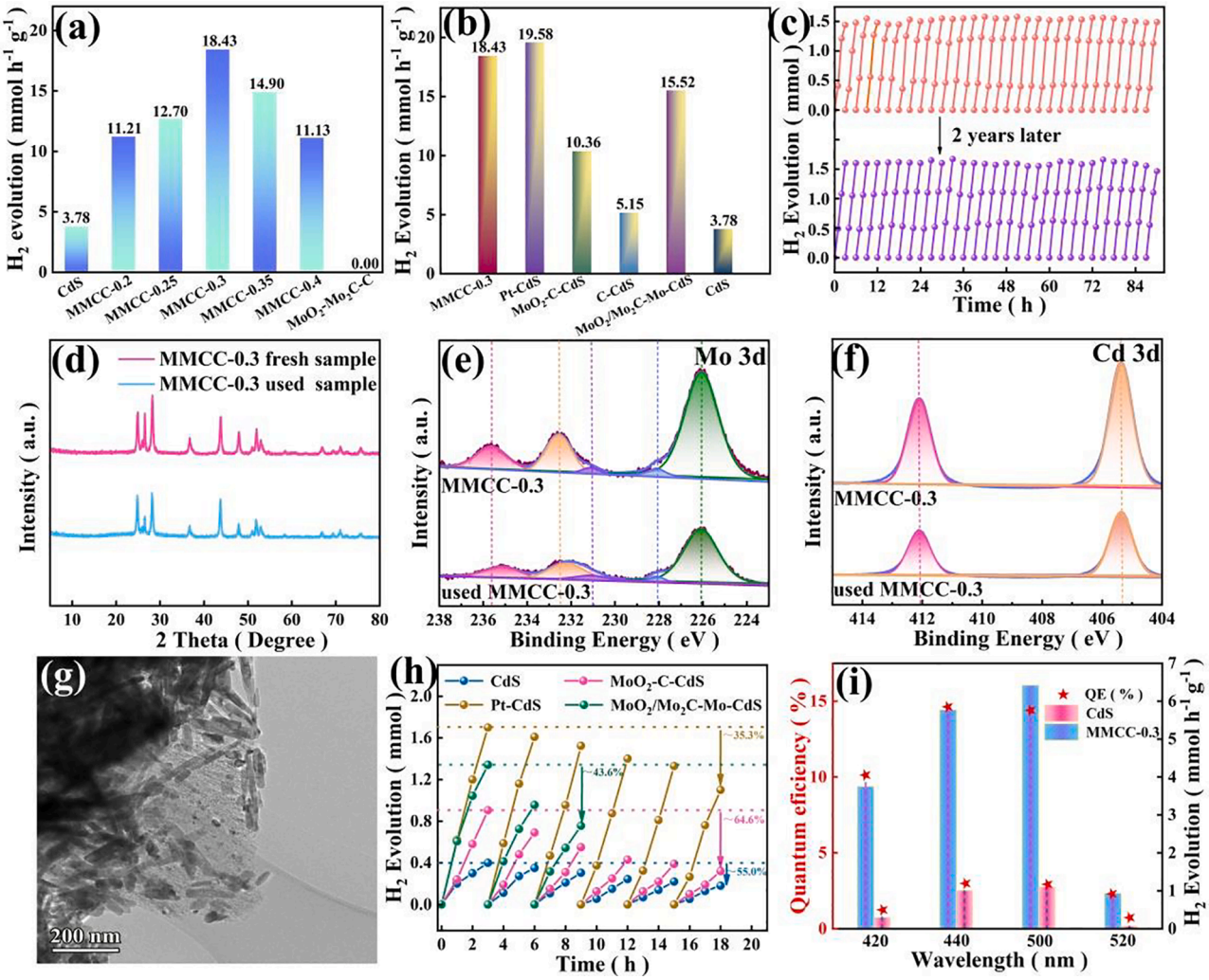

Fig. 6. (a) Photocatalytic H_2 evolution rate of MMCC-x (x = 0.2, 0.25, 0.3, 0.35 and 0.4) photocatalysts under visible light irradiation ($\lambda \geq 420$ nm). (b) Activity comparison of various photocatalysts including MoO_2-C-CdS, MoO_2/Mo_2C-Mo-CdS and C-CdS photocatalyst. (c) Long-term stability tests of MMCC-0.3 photocatalyst. (d) XRD patterns and (e-f) XPS of fresh and used MMCC-0.3 photocatalyst. (g) TEM image of used MMCC-0.3 (h) Comparison of stability of CdS, MoO_2-C-CdS, MoO_2/Mo_2C-Mo-CdS and Pt-CdS samples. (i) Wavelength dependence of AQE and H_2 evolution for MMCC-0.3 and CdS.

intersection point of three extension lines along the curves. The E_{fb} of CdS is estimated to be −1.45 versus the Ag|AgCl electrode, which is equal to −1.23 versus standard hydrogen electrode (NHE). Thus the conduction band (CB) position of CdS is calculated to be −1.23 V, for the fact that the E_{fb} is approximately equal to the CB edge. Hence, the valence band (VB) position of CdS is determined to be 1.07 V based on the empirical formula [72]: $E_{VB} = E_{CB} + E_g$. In addition, ultraviolet photoelectron spectroscopy (UPS) results of CdS and MoO_2/Mo_2C-C are shown in Fig. 8c–f. The band gap between valance bands maximum (VBM) and Fermi level (E_f) of CdS and MoO_2/Mo_2C-C are 1.07 and 1.02 eV, while the cut-off edges for CdS and MoO_2/Mo_2C-C are 15.9 and 15.5 eV, respectively. Thus, the work functions (φ) of CdS and MoO_2/Mo_2C-C are determined to be 5.3 and 5.7 eV according to $\varphi = h\upsilon$-(E_{cutoff} -E_{Fermi}) ($h\upsilon$ = 21.22 eV) [73]. The higher work function of MoO_2/Mo_2C-C indicates the strong electrons withdrawing ability, which could capture electrons from CdS and hence and hence significantly suppress the electron-hole recombination to enhance the photocatalytic H_2 evolution activity of CdS [74].

The charge transfer dynamics was probed by multiple technologies including PL, TPR, SPV and time-resolved fluorescence spectra. PL spectra of all the samples excited at 320 nm are shown in Fig. 9a. After the decoration of MoO_2/Mo_2C-C cocatalyst, the emission intensity of MMCC photocatalyst decreased remarkably, especially for MMCC-0.3 sample, indicating the MoO_2/Mo_2C-C cocatalyst could efficiently promote the separation of charge carriers [75]. TPR in Fig. 9b further reveals the charge separation behavior. For MoO_2/Mo_2C-C cocatalyst, no photocurrent signal is observed for the metallic characters [76,77]. Very weak photocurrent was observed for CdS due to the fast recombination of photo excited electrons and holes. As for MMCC samples, the photocurrent density increased significantly, among which MMCC-0.3 sample shows the highest value for the best electron-hole separation efficiency [78]. Since SPV signal is caused by the surface potential change, the positive photo voltage signals of CdS and MMCC-0.3 are the results of holes accumulation on the sample surface, indicating both of them are *n*-type semiconductors (Fig. 9c). The significantly enhanced SPV signal of MMCC-0.3 can be interpreted by the fact that more holes are accumulated for efficient charge separation [79]. These results prove the electrons and holes are efficiently separated to prolong the electron lifetime, as further decoded by time-resolved fluorescence spectra at 320 nm excitation wavelength in Fig. 9d. The curves are well matched by two-exponential fitting based on the following Eq. (9):

$$I_t = A_1 exp\left(-\frac{t}{\tau_1}\right) + A_2 exp\left(-\frac{t}{\tau_2}\right) \quad (9)$$

where A_1 and A_2 are the contributions of two different processes to the

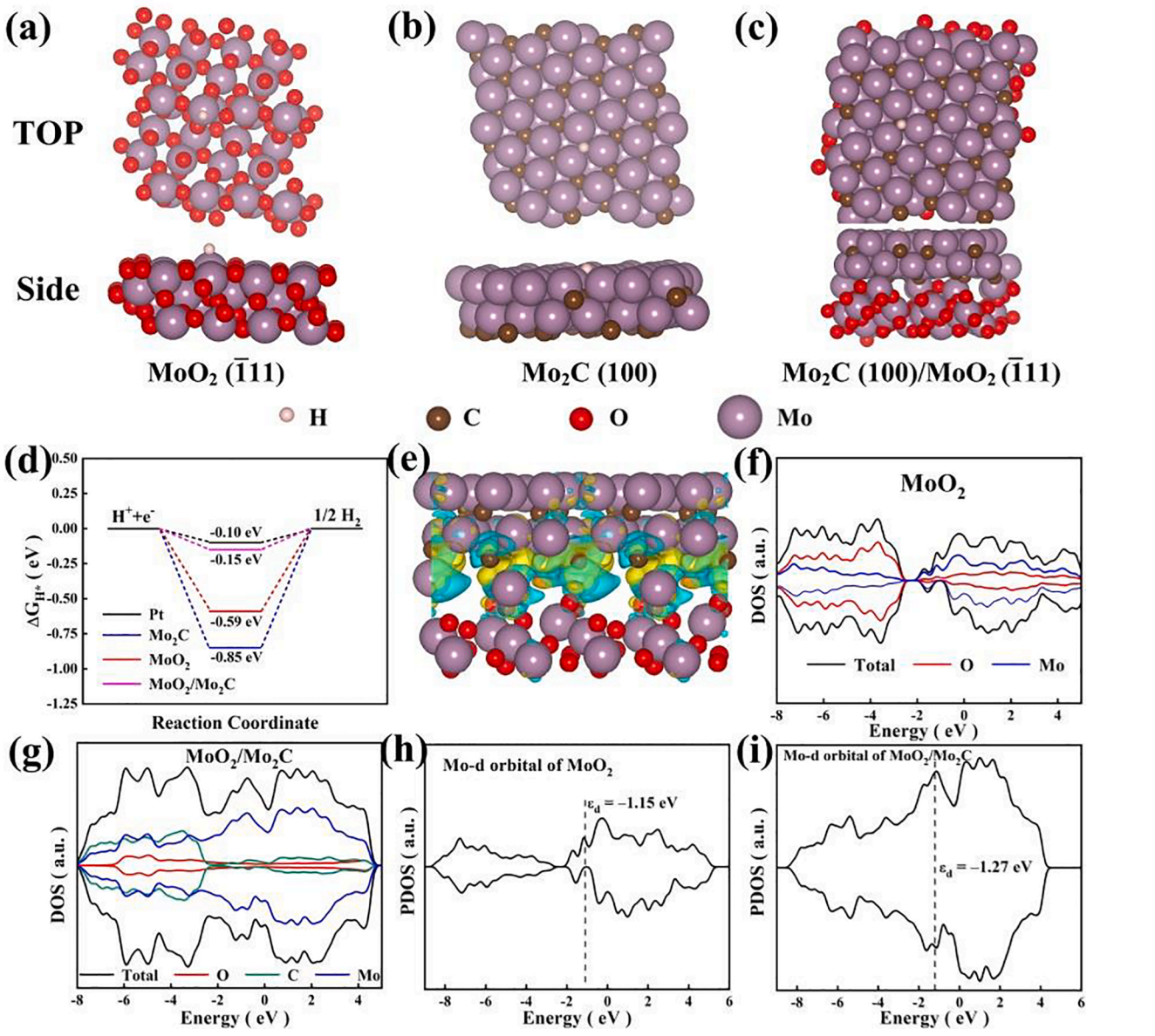

Fig. 7. DFT calculations: The top and side view of the three molecular structure for DFT calculations. (a) MoO_2 ($\bar{1}11$), (b) Mo_2C (100) and (c) Mo_2C (100)/MoO_2 ($\bar{1}11$). d) ΔG_{H^*} on various cocatalyst. e) The differential charge density of MoO_2/Mo_2C. The isovalue of the isosurfaces is 3.0×10^{-3} eÅ^{-3}, yellow and cyan represents the charge accumulation and deletion, respectively. DOS of (f) MoO_2 and (g) MoO_2/Mo_2C. d-band center of MoO_2 (h) and MoO_2/Mo_2C cocatalyst (i).

fluorescence lifetime; the shorter lifetime τ_1 corresponds to the fast quench of carriers trapped at shallow defect states of CdS while longer τ_2 is the lifetime related with the radiative recombination of charge carriers at deeper sites.

The average lifetimes (τ) of photo-excited carriers were determined by Eq. (10):

$$\tau = \frac{A_1\tau_1^2 + A_2\tau_2^2}{A_1\tau_1 + A_2\tau_2} \tag{10}$$

The determined τ_1, τ_2 and average lifetimes (τ) of photo-excited carriers are shown in Table S5. Obviously, compared with bare CdS (τ_1 = 1.23 ns, τ_2 = 3.98 ns), the decay lifetime of MMCC-0.3 photocatalyst (τ_1 = 0.84 ns, τ_2 = 2.61 ns) are significantly decreased for the electrons are rapidly transferred to the MoO_2/Mo_2C-C cocatalyst [80]. Meanwhile, the calculated average decay time of MMCC-0.3 (τ = 2.53 ns) is lower than that of CdS (τ = 3.59 ns), revealing the effective carrier separation by the delocalization of electrons from CdS to MoO_2/Mo_2C-C [81,82]. The suppressed charge recombination was caused by the carbon matrix being fast channel for electrons transfer in the non-radiative recombination pathways, as reported in other works [83,84]. Furthermore, the charge transfer dynamics can be concluded based on the calculated electron transfer rate constants (k_{et}) from Marcus' theory in Eq. (11):

$$k_{et}(\mathrm{MMCC}\rightarrow\mathrm{CdS}) = \frac{1}{\tau(MMCS)} - \frac{1}{\tau(CdS)} \tag{11}$$

The obtained k_{et} associated with electrons transfer from CdS to MoO_2/Mo_2C-C cocatalyst was determined to be 0.8×10^8 s^{-1}. These results indicate the photo-generated electrons were efficiently transferred from CdS to MoO_2/Mo_2C in virtue of the carbon matrix, which significantly contributes to the photocatalytic activity.

The increased charge transfer for MMCC was further verified by Nyquist plot in the EIS and LSV polarization curves [85]. As shown in Fig. 10a, the significantly decreased semicircle radius of MMCC-0.3 manifests the MoO_2/Mo_2C-C cocatalyst could efficiently decrease the interfacial charge transfer resistance and result in efficient charge

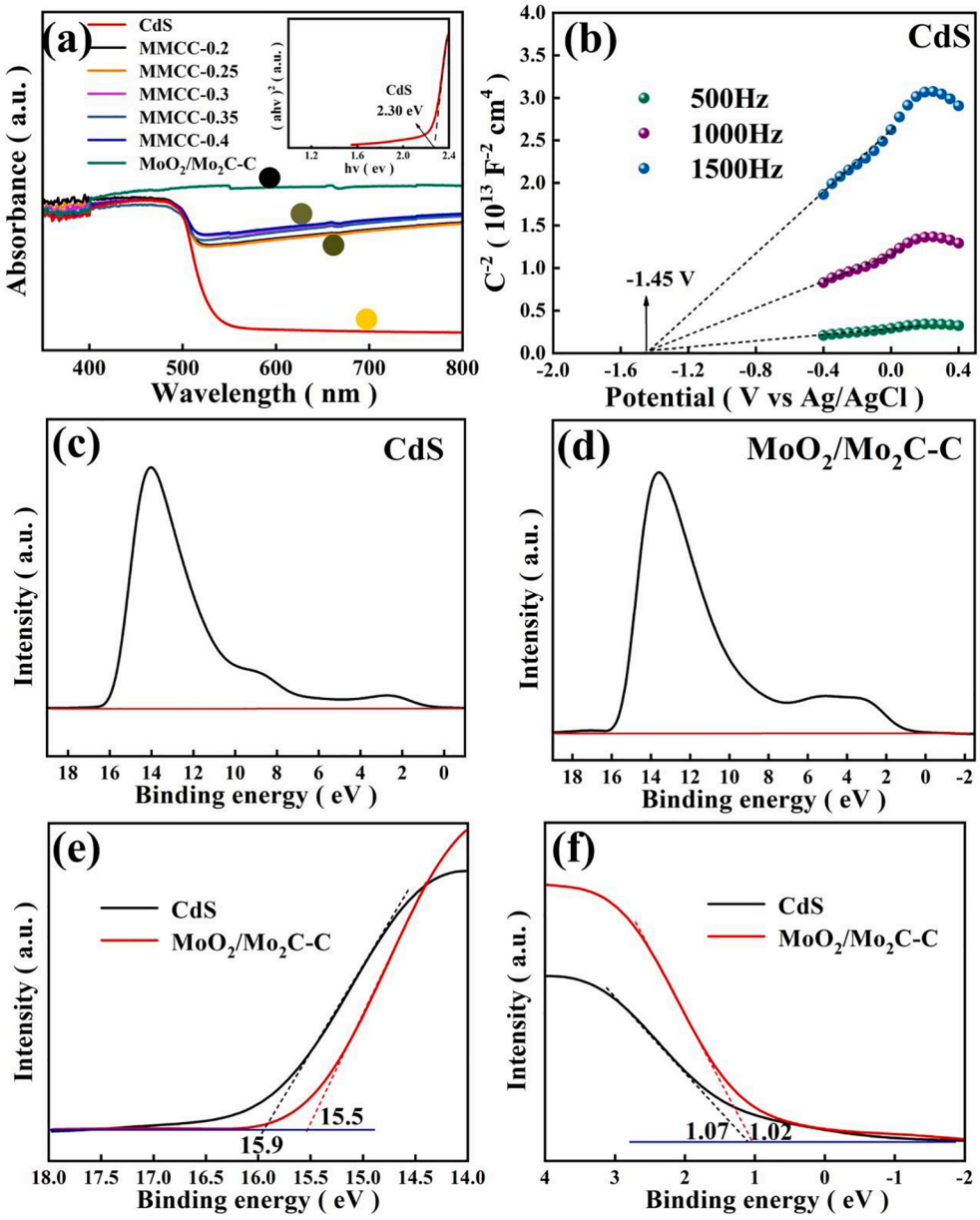

Fig. 8. (a) DRS of CdS, MoO_2/Mo_2C-C, and MMCC samples and the corresponding Tauc plots of UV–vis spectra (inset), (b) M−S curves of CdS under three different frequencies. (c-d) UPS spectra of CdS and MoO_2/Mo_2C-C taken with a photon energy of 21.2 eV, with 0 eV binding energy corresponding to the Fermi level. Zoomed in views of the (e) higher binding energy region and (f) low binding energy region.

carriers' separation, thus ensuring high H_2 evolution efficiency. The roles of MoO_2/Mo_2C-C cocatalyst in the P-HER process are further demonstrated by LSV plots in Fig. 10b. Obviously, MoO_2/Mo_2C-C cocatalyst has the lowest over-potential η_{10}, indicating the superior H proton reduction capacity [86]. Compared with CdS, the η_{10} of MMCC-0.3 sample is much lower due to the decoration of MoO_2/Mo_2C-C cocatalyst, implying that the energy barrier for P-HER of CdS is declined by the loading of MoO_2/Mo_2C-C. Moreover, the smallest Tafel slope for MMCC-0.3 sample (inset of Fig. 10b) reveal that the hydrogen production kinetics is much favorable in comparison with CdS, further demonstrating the fastest kinetic rate.

Based on the results mentioned above, the superior P-HER performance of MMCC photocatalyst could be attributed to the synergistic effect of structure and components, as schematically elaborated in Fig. 11. Under visible light irradiation, majority of the photo-excited electrons on the CB of CdS will pass through carbon matrix and inject into MoO_2/Mo_2C electron reservoir for H_2 evolution. Meanwhile, the holes in the VB of CdS participate in the oxidation reaction of lactic acid. The superior photocatalytic H_2 production activity and excellent stability of the MMCC-0.3 sample could be ascribed to the following aspects: (i) the formation of metallic hybrid MoO_2/Mo_2C heterojunction optimize the electronic structure by adjusting d-band center and hydrogen binding energy ($\triangle G_{H^*}$) to accelerate the H_2-production reaction. (ii) *in-situ* formation of conductive carbon matrix in the cocatalyst not only alleviates the aggregation of MoO_2/Mo_2C cocatalyst to expose abundant active sites but also serves as ideal electron transport bridge to facilitate charge separation. (iii) *in-situ* carburization of MoO_2 by carbon ensured the intimate coupling interaction at the atomic level between MoO_2, Mo_2C and carbon components, thus facilitating the charge transfer rate. (iv) the increased visible light absorption, reduced electron transfer resistance and boosted charge separation ability were realized in a wonderful MMCC photocatalyst.

To further confirm whether the MoO_2/Mo_2C-C is a versatile cocatalyst for other photocatalyst, the MoO_2/Mo_2C-C-TiO_2 and MoO_2/Mo_2C-

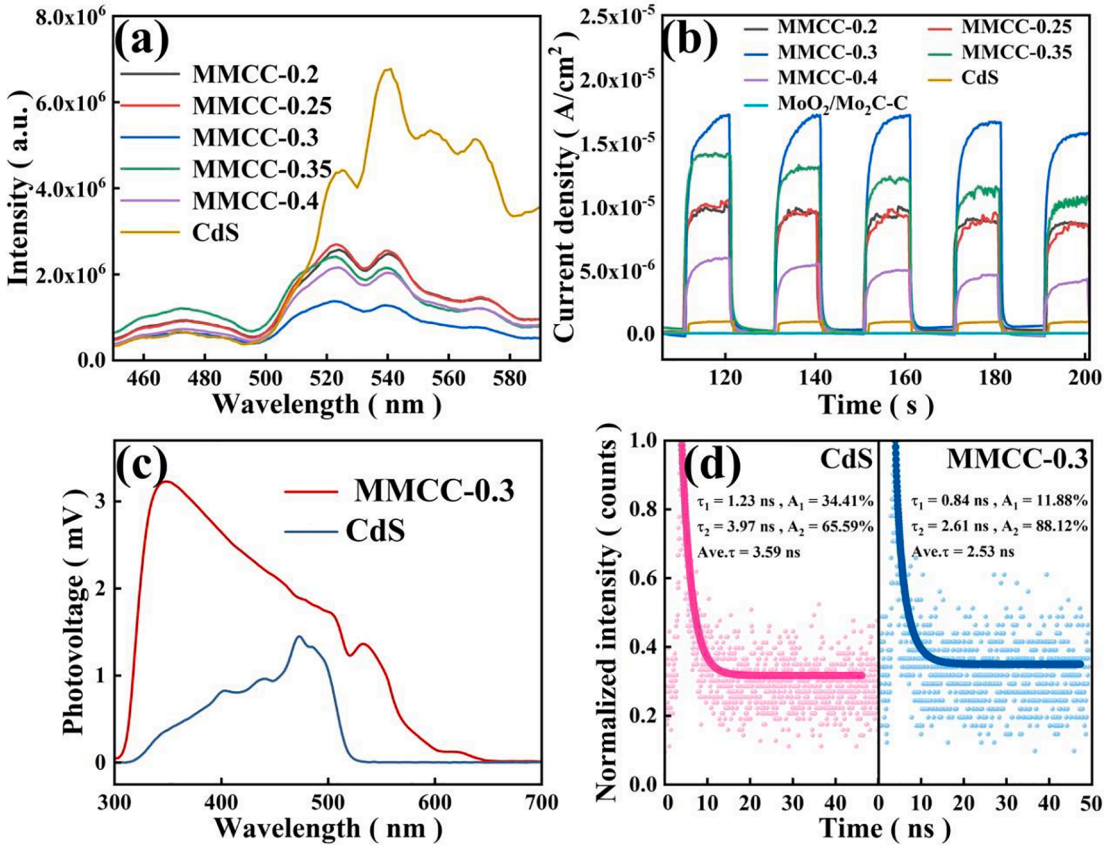

Fig. 9. (a) RT-PL spectra and (b) TPR of the all the samples; (c) SPV and (d) time-resolved fluorescence spectra of CdS and MMCC-0.3.

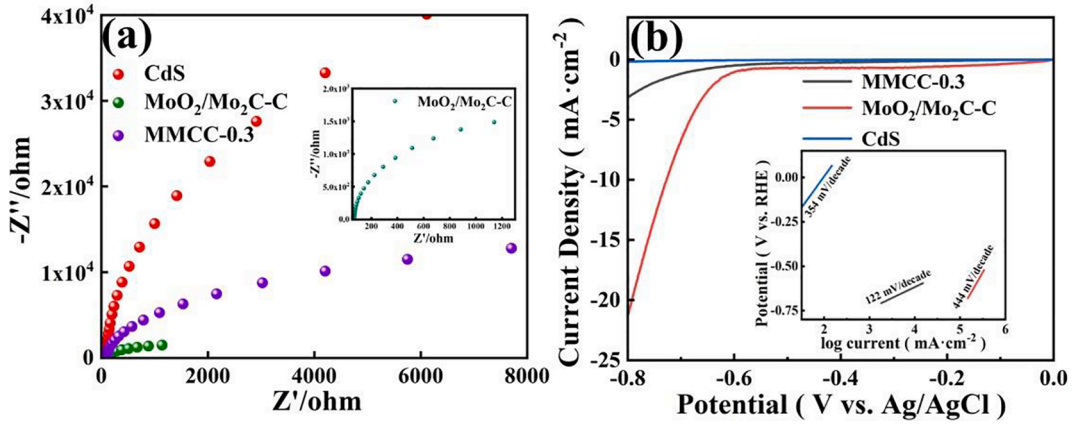

Fig. 10. (a) EIS curves and (b) LSV polarization curves of MoO_2/Mo_2C-C, CdS and MMCC-0.3 samples.

C-$ZnIn_2S_4$ are also prepared by mixing MoO_2/Mo_2C-C with TiO_2 and $ZnIn_2S_4$ under the same condition respectively. The photocatalytic hydrogen evolution rates were tested under full spectrum for MoO_2/Mo_2C-C-TiO_2 and visible light for MoO_2/Mo_2C-C-$ZnIn_2S_4$. As shown in Fig. S12, the hydrogen evolution rates of MoO_2/Mo_2C-C-TiO_2 and MoO_2/Mo_2C-C-$ZnIn_2S_4$ are significantly enhanced than that of pure TiO_2 and $ZnIn_2S_4$, indicating the MoO_2/Mo_2C-C can be used as a universal and efficient cocatalyst for various photocatalysts.

4. Conclusions

In summary, a highly active and super stable MoO_2/Mo_2C-C cocatalyst was successfully constructed for CdS photocatalytic H_2 evolution. The optimized hydrogen binding energy, d-band center and strong electron coupling in hybrid cocatalyst endow MoO_2/Mo_2C-C fantastic cocatalytic activity. Notably, the coupled MoO_2/Mo_2C-C-CdS photocatalyst gives splendid P-HER performance and durability. The synergistic effects of optimized cocatalyst, highly conductive carbon bridge, high quality interface between various components, enhanced light absorption ability and inhibited charge recombination for excellent photocatalytic performance was certified. It is expected that the strategy adopted here provides valuable insight for the construction of other efficient cocatalysts for P-HER performance.

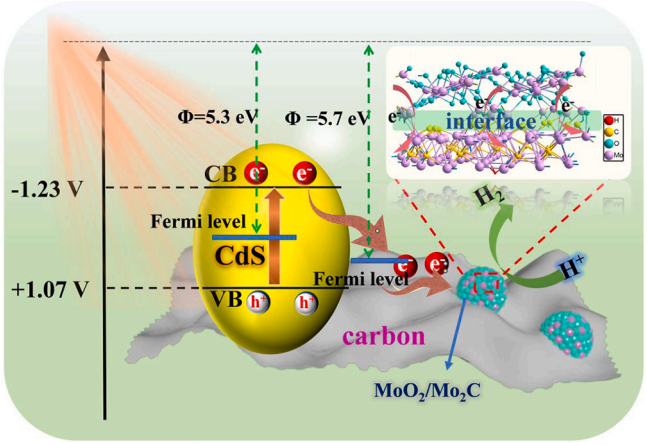

Fig. 11. Illustrative diagram of photocatalytic H_2 evolution over the MMCC photocatalyst.

Declaration of Competing Interest

The authors declare that they have no known competing financial interests or personal relationships that could have appeared to influence the work reported in this paper.

Data availability

The data that has been used is confidential.

Acknowledgements

This work was financially supported by National Natural Science Foundation of China (Nos. 21971143 and 21805165), the Hubei Provincial Department of Education (D20201207) and 111 Project (D20015).

Appendix A. Supplementary data

Supplementary data to this article can be found online at https://doi.org/10.1016/j.cej.2022.140791.

References

[1] J. Hu, T. Yang, X. Yang, J. Qu, Y. Cai, C.M. Li, Highly Selective and efficient solar-light-driven co2 conversion with an ambient-stable 2d/2d co2p@bp/g-c3n4 heterojunction, Small 18 (2021) 2105376.
[2] J. Qi, W. Zhang, R. Cao, Solar-to-hydrogen energy conversion based on water splitting, Adv. Energy Mater. 8 (2018) 1701620.
[3] S. Gong, J. Fan, V. Cecen, C. Huang, Y. Min, Q. Xu, H. Li, Noble-metal and cocatalyst free W_2N/C/TiO photocatalysts for efficient photocatalytic overall water splitting in visible and near-infrared light regions, Chem. Eng. J. 405 (2021), 126913.
[4] J. Hu, C. Chen, H. Yang, F. Yang, J. Qu, X. Yang, W. Sun, L. Dai, C.M. Li, Tailoring well-ordered, highly crystalline carbon nitride nanoarrays via molecular engineering for efficient photosynthesis of H_2O_2, Appl. Catal. B: Environ. 317 (2022), 121723.
[5] D. Gao, J. Xu, F. Chen, P. Wang, H. Yu, Unsaturated selenium-enriched $MoSe_2^+$ amorphous nanoclusters: One-step photoinduced co-reduction route and its boosted photocatalytic H_2-evolution activity for TiO_2, Appl. Catal. B: Environ. 305 (2022), 121053.
[6] M. Zhang, C. Qin, W. Sun, C. Dong, J. Zhong, K. Wu, Y. Ding, Energy funneling and charge separation in CdS modified with dual cocatalysts for enhanced H_2 generation, Chin. J. Catal. 43 (2022) 1818–1829.
[7] X. Li, J. Hu, T. Yang, X. Yang, J. Qu, C.M. Li, Efficient photocatalytic H_2-evolution coupled with valuable furfural-production on exquisite 2D/2D $LaVO_4$/g-C_3N_4 heterostructure, Nano Energy 92 (2022), 106714.
[8] T. Yang, Y. Shao, J. Hu, J. Qu, X. Yang, F. Yang, C. Ming Li, Ultrathin layered 2D/2D heterojunction of ReS_2/high-crystalline g-C_3N_4 for significantly improved photocatalytic hydrogen evolution, Chem. Eng. J. 448 (2022), 137613.
[9] Q. Zhu, B. Qiu, H. Duan, Y. Gong, Z. Qin, B. Shen, M. Xing, J. Zhang, Electron directed migration cooperated with thermodynamic regulation over bimetallic NiFeP/g-C_3N_4 for enhanced photocatalytic hydrogen evolution, Appl. Catal. B: Environ. 259 (2019), 118078.
[10] J. Hu, C. Chen, Y. Zheng, G. Zhang, C. Guo, C.M. Li, Spatially separating redox centers on z-scheme znin2s4/bivo4 hierarchical heterostructure for highly efficient photocatalytic hydrogen evolution, Small 16 (2020) 2002988.
[11] Y.-T. Liu, M.-Y. Lu, T.-P. Perng, L.-J. Chen, Plasmonic enhancement of hydrogen production by water splitting with CdS nanowires protected by metallic TiN overlayers as highly efficient photocatalysts, Nano Energy 89 (2021), 106407.
[12] Q.M. Hui Zhao, L. Jian, Yuming Dong, Yongfa Zhu, Photodeposition of earth-abundant cocatalysts in photocatalytic water splitting: methods, functions, and mechanisms, Chin. J. Catal. 43 (2022) 1774–1804.
[13] X. Han, T. Si, Q. Liu, F. Zhu, R. Li, X. Chen, J. Liu, H. Sun, J. Zhao, H. Ling, Q. Zhang, H. Wang, 2D bimetallic RuNi alloy Co-catalysts remarkably enhanced the photocatalytic H_2 evolution performance of g-C_3N_4 nanosheets, Chem. Eng. J. 426 (2021), 130824.
[14] R. Shen, Y. Ding, S. Li, P. Zhang, Q. Xiang, Y.H. Ng, X. Li, Constructing low-cost Ni_3C/twin-crystal $Zn_{0.5}Cd_{0.5}S$ heterojunction/homojunction nanohybrids for efficient photocatalytic H_2 evolution, Chin. J. Catal. 42 (2021) 25–36.
[15] C. Li, S. Du, H. Wang, S.B. Naghadeh, A.L. Allen, X. Lin, G. Li, Y. Liu, H. Xu, C. He, J.Z. Zhang, P. Fang, Enhanced visible-light-driven photocatalytic hydrogen generation using $NiCo_2S_4$/CdS nanocomposites, Chem. Eng. J. 378 (2019), 122089.
[16] Z. Yin, X. Liu, S. Chen, T. Ma, Y. Li, Interface engineering and anion engineering of Mo-based heterogeneous electrocatalysts for hydrogen evolution reaction, Energy Environ. Mater., doi.org/10.1002/eem2.12310.
[17] L. Zhu, J. Ji, J. Liu, S. Mine, M. Matsuoka, J. Zhang, M. Xing, Designing 3D-MoS_2 sponge as excellent cocatalysts in advanced oxidation processes for pollutant control, Angew. Chem. Int. Ed. 59 (2020) 13968–13976.
[18] J. Ji, Y. Bao, X. Liu, J. Zhang, M. Xing, Molybdenum-based heterogeneous catalysts for the control of environmental pollutants, EcoMat 3 (2021) e12155.
[19] J. Ji, R.M. Aleisa, H. Duan, J. Zhang, Y. Yin, M. Xing, Metallic Active Sites on MoO_2(110) Surface to Catalyze Advanced Oxidation Processes for Efficient Pollutant Removal 23 (2020) 100861.
[20] H. Yu, R. Yuan, D. Gao, Y. Xu, J. Yu, Ethyl acetate-induced formation of amorphous MoSx nanoclusters for improved H_2-evolution activity of TiO_2 photocatalyst, Chem. Eng. J. 375 (2019), 121934.
[21] X.-Q. Qiao, Z.-W. Zhang, F.-Y. Tian, D.-F. Hou, Z.-F. Tian, D.-S. Li, Q. Zhang, Enhanced catalytic reduction of p-nitrophenol on ultrathin mos_2 nanosheets decorated with noble metal nanoparticles, Cryst. Growth Des. 17 (2017) 3538–3547.
[22] X.-Q. Qiao, F.-C. Hu, F.-Y. Tian, D.-F. Hou, D.-S. Li, Equilibrium and kinetic studies on MB adsorption by ultrathin 2D MoS_2 nanosheets, RSC Adv. 6 (2016) 11631–11636.
[23] K. Chen, X.-M. Zhang, X.-F. Yang, M.-G. Jiao, Z. Zhou, M.-H. Zhang, D.-H. Wang, X.-H. Bu, Electronic structure of heterojunction MoO_2/g-C_3N_4 catalyst for oxidative desulfurization, Appl. Catal. B: Environ. 238 (2018) 263–273.
[24] C. Bie, B. Zhu, L. Wang, H. Yu, C. Jiang, T. Chen, J. Yu, A bifunctional cds/moo_2/mos_2 catalyst enhances photocatalytic h_2 evolution and pyruvic acid synthesis, Angew. Chem. Int. Ed. 61 (2022) e202212045.
[25] J. Liu, P. Wang, J. Fan, H. Yu, Carbon-coated cubic-phase molybdenum carbide nanoparticle for enhanced photocatalytic H_2-evolution performance of TiO_2, J. Energy Chem. 51 (2020) 253–261.
[26] J. Liu, P. Wang, J. Fan, H. Yu, J. Yu, In situ synthesis of mo_2c nanoparticles on graphene nanosheets for enhanced photocatalytic h_2-production activity of TiO_2, ACS Sustainable Chem. Eng. 9 (2021) 3828–3837.
[27] L. Gao, J. Liu, H. Long, P. Wang, H. Yu, One-step calcination synthesis of WC–Mo_2C heterojunction nanoparticles as novel H_2-production cocatalysts for enhanced photocatalytic activity of TiO_2, Catal. Sci. Technol. 11 (2021) 7307–7315.
[28] Y.-J. Tang, M.-R. Gao, C.-H. Liu, S.-L. Li, H.-L. Jiang, Y.-Q. Lan, M. Han, S.-H. Yu, Porous molybdenum-based hybrid catalysts for highly efficient hydrogen evolution, Angew. Chem. Int. Ed. 54 (2015) 12928–12932.
[29] W. Tian, H. Hu, Y. Wang, P. Li, J. Liu, J. Liu, X. Wang, X. Xu, Z. Li, Q. Zhao, H. Ning, W. Wu, M. Wu, Metal-organic frameworks mediated synthesis of one-dimensional molybdenum-based/carbon composites for enhanced lithium storage, ACS Nano 12 (2018) 1990–2000.
[30] D. Gao, J. Xu, L. Wang, B. Zhu, H. Yu, J. Yu, Optimizing atomic hydrogen desorption of sulfur-rich nis_{1+x} cocatalyst for boosting photocatalytic h_2 evolution, Adv. Mater. 34 (2021) 2108475.
[31] Z.-W. Zhang, Q.-H. Li, X.-Q. Qiao, D. Hou, D.-S. Li, One-pot hydrothermal synthesis of willow branch-shaped MoS_2/CdS heterojunctions for photocatalytic H_2 production under visible light irradiation, Chin. J. Catal. 40 (2019) 371–379.
[32] Y. Jia, Z. Wang, X.-Q. Qiao, L. Huang, S. Gan, D. Hou, J. Zhao, C. Sun, D.-S. Li, A synergistic effect between S-scheme heterojunction and Noble-metal free cocatalyst to promote the hydrogen evolution of ZnO/CdS/MoS_2 photocatalyst, Chem. Eng. J. 424 (2021), 130368.
[33] G.K.J. Furthmüller, Efficient iterative schemes for ab initio total-energy calculations using a plane-wave basis set, Phys. Rev. B 16 (1996) 11169–11186.
[34] J. Rossmeisl, A. Logadottir, J.K. Nørskov, Electrolysis of water on (oxidized) metal surfaces, Chem. Phys. 319 (2005) 178–184.
[35] E. Picheau, A. Impellizzeri, D. Rybkovskiy, M. Bayle, J.-Y. Mevellec, F. Hof, H. Saadaoui, L. Noé, A.C. Torres Dias, J.-L. Duvail, M. Monthioux, B. Humbert, P. Puech, C.P. Ewels, A. Pénicaud, Intense Raman D Band without Disorder in Flattened Carbon Nanotubes, ACS Nano, 15 (2021) 596-603.
[36] C. Hou, J. Wang, W. Du, J. Wang, Y. Du, C. Liu, J. Zhang, H. Hou, F. Dang, L. Zhao, Z. Guo, One-pot synthesized molybdenum dioxide–molybdenum carbide

heterostructures coupled with 3D holey carbon nanosheets for highly efficient and ultrastable cycling lithium-ion storage, J. Mater. Chem. A 7 (2019) 13460–13472.
[37] L. He, W. Zhang, Q. Mo, W. Huang, L. Yang, Q. Gao, Molybdenum Carbide-Oxide Heterostructures: In Situ Surface Reconfiguration toward Efficient Electrocatalytic Hydrogen Evolution, Angew. Chem. Int. Ed., 59 (2020) 3544-3548.
[38] Y.-L. Men, Y. You, Y.-X. Pan, H. Gao, Y. Xia, D.-G. Cheng, J. Song, D.-X. Cui, N. Wu, Y. Li, S. Xin, J.B. Goodenough, Selective co evolution from photoreduction of co_2 on a metal-carbide-based composite catalyst, J. Am. Chem. Soc. 140 (2018) 13071–13077.
[39] P. Xiao, Y. Yan, X. Ge, Z. Liu, J.-Y. Wang, X. Wang, Investigation of molybdenum carbide nano-rod as an efficient and durable electrocatalyst for hydrogen evolution in acidic and alkaline media, Appl. Catal. B: Environ. 154–155 (2014) 232–237.
[40] Y. Ma, T. Yang, H. Zou, W. Zang, Z. Kou, L. Mao, Y. Feng, L. Shen, S.J. Pennycook, L. Duan, X. Li, J. Wang, Synergizing mo single atoms and mo_2c nanoparticles on cnts synchronizes selectivity and activity of electrocatalytic n_2 reduction to ammonia, Adv. Mater. 32 (2020) e2002177.
[41] T. Li, T. Lu, X. Li, L. Xu, Y. Zhang, Z. Tian, J. Yang, H. Pang, Y. Tang, J. Xue, Atomically dispersed mo sites anchored on multichannel carbon nanofibers toward superior electrocatalytic hydrogen evolution, ACS Nano 15 (2021) 20032–20041.
[42] H. Zhang, P. Zhang, M. Qiu, J. Dong, Y. Zhang, X.W.D. Lou, Ultrasmall MoOx clusters as a novel cocatalyst for photocatalytic hydrogen evolution, Adv. Mater. 31 (2019) e1804883.
[43] K. Chu, Y. Luo, P. Shen, X. Li, Q. Li, Y. Guo, Unveiling the synergy of o-vacancy and heterostructure over moo_{3-x}/mxene for n_2 electroreduction to NH_3, Adv. Energy Mater. 12 (2021) 2103022.
[44] T. Wu, E. Song, S. Zhang, M. Luo, C. Zhao, W. Zhao, J. Liu, F. Huang, Engineering metallic heterostructure based on ni_3n and 2m-mos_2 for alkaline water electrolysis with industry-compatible current density and stability, Adv. Mater. 34 (2022) 2108505.
[45] Z. Shi, K. Nie, Z.-J. Shao, B. Gao, H. Lin, H. Zhang, B. Liu, Y. Wang, Y. Zhang, X. Sun, X.-M. Cao, P. Hu, Q. Gao, Y. Tang, Phosphorus-Mo_2C@carbon nanowires toward efficient electrochemical hydrogen evolution: composition, structural and electronic regulation, Energy Environ. Sci. 10 (2017) 1262–1271.
[46] J. Li, Y. Ye, L. Ye, F. Su, Z. Ma, J. Huang, H. Xie, D.E. Doronkin, A. Zimina, J.-D. Grunwaldt, Y. Zhou, Sunlight induced photo-thermal synergistic catalytic CO_2 conversion via localized surface plasmon resonance of MoO_{3-x}, J. Mater. Chem. A 7 (2019) 2821–2830.
[47] Q. Gao, W. Zhang, Z. Shi, L. Yang, Y. Tang, Structural design and electronic modulation of transition-metal-carbide electrocatalysts toward efficient hydrogen evolution, Adv. Mater. 31 (2019) 1802880.
[48] T. Meng, L. Zheng, J. Qin, D. Zhao, M. Cao, A three-dimensional hierarchically porous Mo_2C architecture: salt-template synthesis of a robust electrocatalyst and anode material towards the hydrogen evolution reaction and lithium storage, J. Mater. Chem. A 5 (2017) 20228–20238.
[49] S. Shen, Z. Wang, Z. Lin, K. Song, Q. Zhang, F. Meng, L. Gu, W. Zhong, Crystalline-amorphous interfaces coupling of $cose_2$/cop with optimized d-band center and boosted electrocatalytic hydrogen evolution, Adv. Mater. 34 (2022) 2110631.
[50] J. Cai, J. Ding, D. Wei, X. Xie, B. Li, S. Lu, J. Zhang, Y. Liu, Q. Cai, S. Zang, Coupling of ru and o-vacancy on 2d mo-based electrocatalyst via a solid-phase interface reaction strategy for hydrogen evolution reaction, Adv. Energy Mater. 11 (2021) 2100141.
[51] L. Chen, H. Jiang, H. Jiang, H. Zhang, S. Guo, Y. Hu, C. Li, Mo-based ultrasmall nanoparticles on hierarchical carbon nanosheets for superior lithium ion storage and hydrogen generation catalysis, Adv. Energy Mater. 7 (2017) 1602782.
[52] D. Zhang, W. Liu, R. Wang, Z. Zhang, S. Qiu, Interface engineering of hierarchical photocatalyst for enhancing photoinduced charge transfers, Appl. Catal. B: Environ. 283 (2021), 119632.
[53] Z. Xu, G. Zhang, C. Lu, H. Tian, X. Xi, R. Liu, D. Wu, Molybdenum carbide nanoparticle decorated hierarchical tubular carbon superstructures with vertical nanosheet arrays for efficient hydrogen evolution, J. Mater. Chem. A 6 (2018) 18833–18838.
[54] X.-Q. Qiao, Z.-W. Zhang, Q.-H. Li, D. Hou, Q. Zhang, J. Zhang, D.-S. Li, P. Feng, X. Bu, In situ synthesis of n–n Bi_2MoO_6 & Bi_2S_3 heterojunctions for highly efficient photocatalytic removal of Cr(vi), J. Mater. Chem. A 6 (2018) 22580–22589.
[55] J. Dong, Q. Wu, C. Huang, W. Yao, Q. Xu, Cost effective Mo rich Mo_2C electrocatalysts for the hydrogen evolution reaction, J. Mater. Chem. A 6 (2018) 10028–10035.
[56] X. Liu, L. Yang, M. Huang, Q. Li, L. Zhao, Y. Sang, X. Zhang, Z. Zhao, H. Liu, W. Zhou, Oxygen vacancy-regulated metallic semiconductor MoO_2 nanobelt photoelectron and hot electron self-coupling for photocatalytic CO_2 reduction in pure water, Appl. Catal. B: Environ. 319 (2022), 121887.
[57] W. Fan, H. Li, F. Zhao, X. Xiao, Y. Huang, H. Ji, Y. Tong, Boosting the photocatalytic performance of (001) BiOI: enhancing donor density and separation efficiency of photogenerated electrons and holes, Chem. Commun. 52 (2016) 5316–5319.
[58] Y. Jia, Z. Wang, X.-Q. Qiao, L. Huang, S. Gan, D. Hou, D.-S. Li, Two dimensional ultrathin $MoSe_2$ bedecked $Zn_{0.5}Cd_{0.5}S$ for reinforced photocatalytic H_2 generation and toxic Cr (VI) reduction, Appl. Surf. Sci. 554 (2021), 149649.
[59] X.-Q. Qiao, Z.-W. Zhang, D.-F. Hou, D.-S. Li, Y. Liu, Y.-Q. Lan, J. Zhang, P. Feng, X. Bu, Tunable mos_2/sno_2 p-n heterojunctions for an efficient trimethylamine gas sensor and 4-nitrophenol reduction catalyst, ACS Sustainable Chem. Eng. 6 (2018) 12375–12384.
[60] Q. Li, X.-Q. Qiao, Y. Jia, D. Hou, D.-S. Li, Amorphous $comos_4$ nanostructure for photocatalytic h2 generation, nitrophenol reduction, and methylene blue adsorption, ACS Appl. Nano Mater. 3 (2020) 68–76.
[61] C. Li, H. Che, Y. Yan, C. Liu, H. Dong, Z-scheme $AgVO_3$/$ZnIn_2S_4$ photocatalysts: "One Stone and Two Birds" strategy to solve photocorrosion and improve the photocatalytic activity and stability, Chem. Eng. J. 398 (2020), 125523.
[62] X. Zhou, Y. Tian, J. Luo, B. Jin, Z. Wu, X. Ning, L. Zhan, X. Fan, T. Zhou, S. Zhang, X. Zhou, MoC quantum dots@n-doped-carbon for low-cost and efficient hydrogen evolution reaction: from electrocatalysis to photocatalysis, Adv. Funct. Mater. 2201518 (2022).
[63] H. Yin, Z. Chen, Y. Peng, S. Xiong, Y. Li, H. Yamashita, J. Li, Dual active centers bridged by oxygen vacancies of ruthenium single-atom hybrids supported on molybdenum oxide for photocatalytic ammonia synthesis, Angew. Chem. Int. Ed. (2022) e202114242.
[64] T. Wang, L. Chen, C. Chen, M. Huang, Y. Huang, S. Liu, B. Li, Engineering catalytic interfaces in $cu^{\delta+}$/ceo_2-tio_2 photocatalysts for synergistically boosting co_2 reduction to ethylene, ACS Nano 16 (2022) 2306–2318.
[65] Y. Wang, X. Li, M. Zhang, J. Zhang, Z. Chen, X. Zheng, Z. Tian, N. Zhao, X. Han, K. Zaghib, Y. Wang, Y. Deng, W. Hu, Highly active and durable single-atom tungsten-doped $nis_{0.5}se_{0.5}$ nanosheet @ $nis_{0.5}se_{0.5}$ nanorod heterostructures for water splitting, Adv. Mater. 34 (2022) 2107053.
[66] X. Liu, Y. Zhao, X. Yang, Q. Liu, X. Yu, Y. Li, H. Tang, T. Zhang, Porous Ni_5P_4 as a promising cocatalyst for boosting the photocatalytic hydrogen evolution reaction performance, Appl. Catal. B: Environ. 275 (2020), 119144.
[67] L. Zeng, K. Sun, X. Wang, Y. Liu, Y. Pan, Z. Liu, D. Cao, Y. Song, S. Liu, C. Liu, Three-dimensional-networked Ni_2P/Ni_3S_2 heteronanoflake arrays for highly enhanced electrochemical overall-water-splitting activity, Nano Energy 51 (2018) 26–36.
[68] Z. Chen, Y. Song, J. Cai, X. Zheng, D. Han, Y. Wu, Y. Zang, S. Niu, Y. Liu, J. Zhu, X. Liu, G. Wang, Tailoring the d-Band centers enables co_4n nanosheets to be highly active for hydrogen evolution catalysis, Angew. Chem. Int. Ed. 57 (2018) 5076–5080.
[69] X. Sun, L. Sun, G. Li, Y. Tuo, C. Ye, J. Yang, J. Low, X. Yu, J.H. Bitter, Y. Lei, D. Wang, Y. Li, Phosphorus tailors the d-band center of copper atomic sites for efficient co_2 photoreduction under visible-light irradiation, Angew. Chem. Int. Ed. (2022) e202207677.
[70] S. Ma, J. Xie, K. He, W. Liu, X. Chen, X. Li, Noble-metal-free Ni_3C cocatalysts decorated CdS nanosheets for high-efficiency visible-light-driven photocatalytic H_2 evolution, Appl. Catal. B: Environ. 227 (2018) 218–228.
[71] F.-Y. Tian, D. Hou, F. Tang, M. Deng, X.-Q. Qiao, Q. Zhang, T. Wu, D.-S. Li, Novel $Zn_{0.8}Cd_{0.2}S$@g-C_3N_4 core–shell heterojunctions with a twin structure for enhanced visible-light-driven photocatalytic hydrogen generation, J. Mater. Chem. A 6 (2018) 17086–17094.
[72] Q. Li, X.-Q. Qiao, Y. Jia, D. Hou, D.-S. Li, Noble-metal-free amorphous CoMoSx modified CdS core-shell nanowires for dramatically enhanced photocatalytic hydrogen evolution under visible light irradiation, Appl. Surf. Sci. 498 (2019), 143863.
[73] Q. Liu, C. Zeng, Z. Xie, L. Ai, Y. Liu, Q. Zhou, J. Jiang, H. Sun, S. Wang, Cobalt@nitrogen-doped bamboo-structured carbon nanotube to boost photocatalytic hydrogen evolution on carbon nitride, Appl. Catal. B: Environ. 254 (2019) 443–451.
[74] R. Shen, J. Xie, Q. Xiang, X. Chen, J. Jiang, X. Li, Ni-based photocatalytic H_2-production cocatalysts, Chin. J. Catal. 40 (2019) 240–288.
[75] J. Peng, J. Shen, X. Yu, H. Tang, Q.L. Zulfiqar, Construction of LSPR-enhanced 0D/2D CdS/MoO_3− S-scheme heterojunctions for visible-light-driven photocatalytic H_2 evolution, Chin. J. Catal. 42 (2021) 87–96.
[76] Y. Song, N. Li, D. Chen, Q. Xu, H. Li, J. He, J. Lu, 3D ordered MoP inverse opals deposited with CdS quantum dots for enhanced visible light photocatalytic activity, Appl. Catal. B: Environ. 238 (2018) 255–262.
[77] W. Wang, T. An, G. Li, D. Xia, H. Zhao, J.C. Yu, P.K. Wong, Earth-abundant Ni_2P/g-C_3N_4 lamellar nanohydrids for enhanced photocatalytic hydrogen evolution and bacterial inactivation under visible light irradiation, Appl. Catal. B: Environ. 217 (2017) 570–580.
[78] S. Nishioka, K. Shibata, Y. Miseki, K. Sayama, K. Maeda, Visible-light-driven nonsacrificial hydrogen evolution by modified carbon nitride photocatalysts, Chin. J. Catal. 43 (2022) 2316–2320.
[79] X. Meng, J. Yang, S. Xu, C. Zhang, B. Ma, Y. Ding, Integrating Mo_2B_x (x = 1, 4) with CdS for efficient photocatalytic hydrogen production, Chem. Eng. J. 410 (2021), 128339.
[80] Y. Sun, C. Xu, H. Ma, G. Li, L. Chen, Y. Sun, Z. Chen, P. Fang, Q. Fu, C. Pan, Synthesis of flower-liked twin crystal ternary Ni/NiS/$Zn0_{.2}Cd_{0.8}S$ catalyst for highly efficient hydrogen production, Chem. Eng. J. 406 (2021), 126878.
[81] Q. Wu, J. Cao, X. Wang, Y. Liu, Y. Zhao, H. Wang, Y. Liu, H. Huang, F. Liao, M. Shao, Z. Kang, A metal-free photocatalyst for highly efficient hydrogen peroxide photoproduction in real seawater, Nat. Commun. 12 (2021) 483.
[82] S. Tang, Y. Xia, J. Fan, B. Cheng, J. Yu, W. Ho, Enhanced photocatalytic H_2 production performance of CdS hollow spheres using C and Pt as bi-cocatalysts, Chin. J. Catal. 42 (2021) 743–752.
[83] M.-Q. Yang, Y.-J. Xu, W. Lu, K. Zeng, H. Zhu, Q.-H. Xu, G.W. Ho, Self-surface charge exfoliation and electrostatically coordinated 2D hetero-layered hybrids, Nat. Commun. 8 (2017) 14224.

[84] F. Liu, R. Shi, Z. Wang, Y. Weng, C.M. Che, Y. Chen, Direct Z-Scheme hetero-phase junction of black/red phosphorus for photocatalytic water splitting, Angew. Chem. Int. Ed. 58 (2019) 11791–11795.

[85] A. Wang, L. Zhang, X. Li, Y. Gao, N. Li, G. Lu, L. Ge, Synthesis of ternary Ni_2P@UiO-66-NH_2/$Zn_{0.5}Cd_{0.5}S$ composite materials with significantly improved photocatalytic H_2 production performance, Chin. J. Catal. 43 (2022) 1295–1305.

[86] P. Wang, S. Xu, F. Chen, H. Yu, Ni nanoparticles as electron-transfer mediators and NiS as interfacial active sites for coordinative enhancement of H_2-evolution performance of TiO_2, Chin. J. Catal. 40 (2019) 343–351.